AGU PUBLICATIONS

JGR

Journal of Geophysical Research: Oceans

RESEARCH ARTICLE

10.1002/2016JC012671

Special Section:
Dense Water Formations in the North Western Mediterranean: From the Physical Forcings to the Biogeochemical Consequences

Multiscale Observations of Deep Convection in the Northwestern Mediterranean Sea During Winter 2012–2013 Using Multiple Platforms

Pierre Testor[1], Anthony Bosse[2], Loïc Houpert[3], Félix Margirier[1], Laurent Mortier[4], Hervé Legoff[1], Denis Dausse[1], Matthieu Labaste[1], Johannes Karstensen[5], Daniel Hayes[6], Antonio Olita[7], Alberto Ribotti[7], Katrin Schroeder[8], Jacopo Chiggiato[8], Reiner Onken[9], Emma Heslop[10], Baptiste Mourre[10], Fabrizio D'ortenzio[11], Nicolas Mayot[11], Héloise Lavigne[11], Orens de Fommervault[11,12], Laurent Coppola[11], Louis Prieur[11], Vincent Taillandier[11], Xavier Durrieu de Madron[13], Francois Bourrin[13], Gael Many[13], Pierre Damien[14], Claude Estournel[14], Patrick Marsaleix[14], Isabelle Taupier-Letage[15], Patrick Raimbault[15], Robin Waldman[16], Marie-Noelle Bouin[16,17], Hervé Giordani[16], Guy Caniaux[16], Samuel Somot[16], Véronique Ducrocq[16], and Pascal Conan[18]

[1]CNRS-Sorbonne Universités (UPMC Univ. Pierre et Marie Curie, Paris 06)-CNRS-IRD-MNHN, UMR 7159, Laboratoire d'Océanographie et de Climatologie (LOCEAN), Institut Pierre Simon Laplace (IPSL), Observatoire Ecce Terra, Paris, France, [2]Geophysical Institute, University of Bergen and Bjerknes Center for Climate Research, Bergen, Norway, [3]Scottish Association for Marine Science, Oban, Argyll, Scotland, [4]ENSTA–Paristech, Laboratoire d'Océanographie et de Climatologie (LOCEAN), Palaiseau, France, [5]GEOMAR, Kiel, Germany, [6]Oceanography Center, University of Cyprus, Nicosia, Cyprus, [7]Consiglio Nazionale delle Ricerche - Istituto per l'ambiente Marino Costiero (CNR-IAMC) Oristano, Oristano, Italy, [8]Consiglio Nazionale delle Ricerche - Istituto di Scienze Marine (CNR-ISMAR), Venezia, Italy, [9]Helmholtz-Zentrum Geesthacht, Geesthacht, Germany, [10]SOCIB, Mallorca, Spain, [11]Sorbonne Universités (UPMC Univ. Pierre et Marie Curie, Paris 06), UMR 7093, Laboratoire d'Océanographie de Villefranche (LOV), Observatoire Océanologique de Villefranche/mer, France, [12]Departamento de Oceanografa Fisica, Centro de Investigacion Cientfica y de Educacion Superior de Ensenada, Ensenada, Baja California, Mexico, [13]CNRS-Université de Perpignan, Centre de Formation et de Recherche sur les Environnements Mditerranens (CEFREM), Perpignan, France, [14]CNRS-Universit de Toulouse, Laboratoire d'Aerologie (LA), Observatoire Midi-Pyrénées, Toulouse, France, [15]Aix-Marseille Université, Université de Toulon, CNRS, IRD, MIO UM 110, Marseille, France, [16]MétéoFrance/CNRS, CNRM, UMR 3589, Toulouse, France, [17]Ifremer-CNRS-IRD-UBO, LOPS, IUEM, Plouzané, France, [18]Sorbonne Universités (UPMC Univ. Pierre et Marie Curie, Paris 06), UMR 7093, Laboratoire d'Océanographie Microbienne (LOMIC), Observatoire Océanologique de Banyuls/mer, France

Abstract During winter 2012–2013, open-ocean deep convection which is a major driver for the thermohaline circulation and ventilation of the ocean, occurred in the Gulf of Lions (Northwestern Mediterranean Sea) and has been thoroughly documented thanks in particular to the deployment of several gliders, Argo profiling floats, several dedicated ship cruises, and a mooring array during a period of about a year. Thanks to these intense observational efforts, we show that deep convection reached the bottom in winter early in February 2013 in a area of maximum $28 \pm 3\ 10^9 m^2$. We present new quantitative results with estimates of heat and salt content at the subbasin scale at different time scales (on the seasonal scale to a 10 days basis) through optimal interpolation techniques, and robust estimates of the deep water formation rate of 2.0 ± 0.2 Sv. We provide an overview of the spatiotemporal coverage that has been reached throughout the seasons this year and we highlight some results based on data analysis and numerical modeling that are presented in this special issue. They concern key circulation features for the deep convection and the subsequent bloom such as Submesoscale Coherent Vortices (SCVs), the plumes, and symmetric instability at the edge of the deep convection area.

Key Points:
- We study deep convection and subsequent bloom in the northwestern Mediterranean Sea based on modern observation techniques
- We provide estimates of mass and energy fluxes over a period of a year in the deep convection area and deep water formation rates
- We highlight small-scale circulation features that are important for deep convection and subsequent bloom and introduce this special issue

Correspondence to:
P. Testor,
testor@locean-ipsl.upmc.fr

Citation:
Testor, P., Bosse, A., Houpert, L., Margirier, F., Mortier, L., Legoff, H., . . . Conan, P. (2018). Multiscale observations of deep convection in the northwestern Mediterranean Sea during winter 2012–2013 using multiple platforms. *Journal of Geophysical Research: Oceans*, *123*, 1745–1776. https://doi.org/10.1002/2016JC012671

Received 30 DEC 2016
Accepted 15 NOV 2017
Accepted article online 14 DEC 2017
Published online 5 MAR 2018

1. Introduction

Open-ocean deep convection is a key process that materially exchanges heat and salt, as well as momentum, between the surface layers and the deep ocean in localized regions of the global ocean and is a major contributor to the thermohaline circulation (Marshall & Schott, 1999). Open-ocean deep convection happens in winter and results in oceanic deep water formation. The Mediterranean Sea, the Weddell Sea, the

Labrador Sea, and the Greenland Sea are deep convection areas that are relatively well-documented but many details about what is occurring during the different phases of convection and what drives the vernal bloom that can be observed during the restratification phase are still unclear because many scales appear to interplay and the vertical dimension is difficult to observe.

Deep convection in the Gulf of Lion was first described by the MEDOC-Group (1970) in three phases:

1. the preconditioning of the area by a cyclonic gyre circulation in the whole northwestern Mediterranean Sea producing a doming of isopycnals toward the surface centered at about (42°N, 5°E), exposing a large body of weakly stratified waters to local cooling and evaporation, due to dry and cold Mistral and Tramontane winds blowing over the Gulf of Lion;
2. the vertical mixing due to buoyancy loss generated by intense surface cooling and evaporation reaching about 1,000 W m^{-2} for short periods and allowing overturning of the water column; and
3. the spreading/restratification phase with newly formed deep waters propagating away from the formation site while stratified waters around invade the deep convection area.

This framework is still commonly used in all studies concerning deep convection processes, in all locations of deep water formation, likely because it clearly depicts the major physical drivers. Furthermore, it is well-known winter mixing, and in particular deep convection, participates to transfers of biogeochemical properties like oxygen, all inorganic and organic, dissolved and particulate, matters and is a major contributor to the functioning of the upper ocean ecosystem by supplying in particular nutrients from the deep ocean to the euphotic layer. Convection is one of the major drivers of the phytoplankton phenology (Lavigne et al., 2013) as well as of the deep pelagic and benthic ecosystems (Pusceddu et al., 2010; Stabholz et al., 2013; Tamburini et al., 2013). Satellite ocean color images show high phytoplankton abundances at the surface, starting and increasing during the violent mixing periods around a "blue hole" where deep mixing occurs and then at the subbasin scale during restratification events, generally in April. This is the onset of the most intense bloom in the Mediterranean Sea. As such, it appears to be a major phenomenon for the evolution of the Mediterranean Sea that contributes to the evolution of this physical-biological system, which is considered as a hot spot for biodiversity and climate change (Coll et al., 2010; Giorgi, 2006). The northwestern Mediterranean Sea is well-known to be subject to rapid and drastic responses to climate change (Cacho et al., 2002; Somot et al., 2006), and it is today of the ultimate importance to better understand the response of the Mediterranean water cycle (Adloff et al., 2015) and marine ecosystems to external constraints (Auger et al., 2014; Herrmann et al., 2013, 2014).

From a biogeochemical perspective, the Mediterranean has long been known as an oligotrophic area with relatively low nutrient concentrations, characterized by a general West to East gradient of increasing oligotrophy. The elemental stoichiometry in all compartments (i.e., particulate and dissolved inorganic and organic) reveals an excess of carbon, a deficiency in phosphorus relative to nitrogen, and a sporadic silicate deficiency (Béthoux et al., 2002) as compared to other oceanic provinces. It is well-known that the elemental composition of biotic and abiotic compartments can widely vary with environmental conditions (light, temperature, trophic status), or growth rate of living organisms (Conan et al., 2007), but the Mediterranean anomalies, though frequently explored, still represent open issues for the understanding of the functioning of the marine ecosystem in general. Macronutrient concentrations there depend on the exchanges through the Straits of Gibraltar and Bosphorus, atmospheric depositions, and river discharges, whereas their distributions are controlled by both physical (i.e., dense water formation) and biological activities (consumption/mineralization). Continental inputs are characterized by a strong variability in terms of quantity and quality, dominated by extreme events (i.e., large river floods and dust deposits), due to the climatic specificity of this region. These inputs, lateral fluxes, and the exchanges between the surface and deep layers across the nutriclines, are dominant processes for the development of phytoplankton and higher trophic levels.

From a physical point of view, the violent atmospheric forcing events that trigger deep convection in the center of the preconditioned area (Herrmann & Somot, 2008; Somot et al., 2016) produce a *Mixed Patch* that is unstable. Many studies have shown the important role of baroclinic instability for deep convection (Gascard, 1978; Jones & Marshall, 1997; Killworth, 1976, 1979; Legg et al., 1998; Legg & Marshall, 1993; Testor & Gascard, 2006; Visbeck et al., 1996) because it is a mechanism that could occur throughout the deep convection process, from the preconditioning to the spreading phase, that can contribute to vertical mixing by inducing vertical velocities order of 1–100 m d^{-1} over periods of days, as well as to lateral fluxes by eddy

shedding. At a later stage, once the atmospheric forcing had considerably lessened, the *Mixed Patch* becomes highly unstable and there is a general breakup on a time scale of a few weeks (Madec et al., 1991). Many observations of Submesoscale Coherent Vortices (SCVs as introduced by McWilliams, 1985) of a scale O(5 km) composed of newly formed waters (Gascard et al., 2002; Lilly et al., 1999; Testor & Gascard, 2003, 2006) document the eddy field in such areas and this scale likely modulates the variability in the vicinity of the *Mixed Patch* presenting a horizontal scale of O(100 km). All these SCVs appear to have similar characteristics (small radius, large aspect ratio, and long lifetime of the order of a year). They are involved in the large-scale circulation of the newly formed deep waters (spreading phase) and contribute to the deep ventilation. It appears these vortices are numerous, can travel 100s of km during their lifetime and can export waters composing their cores over long distances and periods of time.

In the *Mixed Patch*, intense vertical velocities O(10 cm s^{-1}) were observed in cells with horizontal and vertical scales of O(1 km) (Schott et al., 1996; Schott & Leaman, 1991) at a smaller scale than the observed eddies. Supported by numerical modeling and tank experiments (Marshall & Schott, 1999) could explain these so-called *plumes* resulting from hydrostatic instability and earth rotation. The *Mixed Patch* would result from an integral effect of these nonpenetrative *plumes* (Send & Marshall, 1995) balanced by lateral buoyancy fluxes. However, these experiments considered a homogeneous ocean forced by a heterogeneous atmosphere (disc-shaped atmospheric forcing) and did not account for preconditioning effects at large, mesoscale or even submesoscale. On the other hand, Legg and McWilliams (2001) proposed that the homogenization of the newly formed deep waters was likely due to the turbulent geostrophic eddy field, and eddies presenting a doming of isopycnals toward the surface could definitely act as local preconditioners favoring locally deep convection.

It is clear that physical and biogeochemical processes act in setting up the Spring bloom that is observed after deep convection events. Vertical and horizontal fluxes of particulate and dissolved inorganic and organic matters are constrained by physical processes and biogeochemical cycles. However, little is known of the scales at which these processes interact and most of the questions that are still unresolved concerning Mediterranean biogeochemical evolution deal with the temporal variability of the key processes that govern the functioning and budgets of the different physical, chemical, and biological compartments.

Observational limits are the principal causes of this uncertainty. The preconditioning, violent mixing, and restratification/spreading phases do overlap with a preconditioning phase starting at least the previous Summer and a spreading phase extending possibly over years, while presenting high-frequency variability. The *Mixed Patch* extends over 100 km with modulations at (sub)mesoscale O(5 km) and small-scale O(1 km) while the bloom seems to extend over the whole northwestern basin with high variability at meso/submeso/small scale, often clearly coupled to the physical one. According to (Durrieu de Madron et al., 2011), bloom and deep convection events result from an "history" of at least 6–8 months beforehand that needs to be characterized. This observational challenge motivated a multiplatform experiment aiming at a continuous description of the water column at the basin/meso/submeso scales over a year. Building on long-term observational efforts in that area, additional observations were carried out in 2012–2013 to try to achieve this goal.

In the present paper, we will describe and analyze the results obtained from this 2012–2013 DEWEX (DEnse Water EXperiment) experiment coordinating different projects in that area, providing a more complete and extended description of the different phases of deep convection. We will first describe the sampling strategy of the experiment and the area under study, based on all in situ potential temperature, salinity, potential density, and fluorescence of chl-a profiles as well as currents and depth-average currents estimates that were collected in this framework thanks to ships, gliders, moorings, profiling floats, and surface drifters. We will provide an overview of the spatiotemporal coverage that was achieved during this experiment, describe the evolution of the northwestern Mediterranean Sea mainly from a physical point of view, and estimate newly formed deep water formation rates and energy fluxes. We will finally discuss the importance of different physical processes for the deep convection and subsequent bloom, that were observed during our study period based on different studies developed in this framework, before a general conclusion.

2. The Multiplatform Sampling Strategy

Taking advantage of long-term observational efforts (Long-term Observation Period, LOP) carried out in the framework of MOOSE (Mediterranean Ocean Observing System for the Environment, http://www.moose-

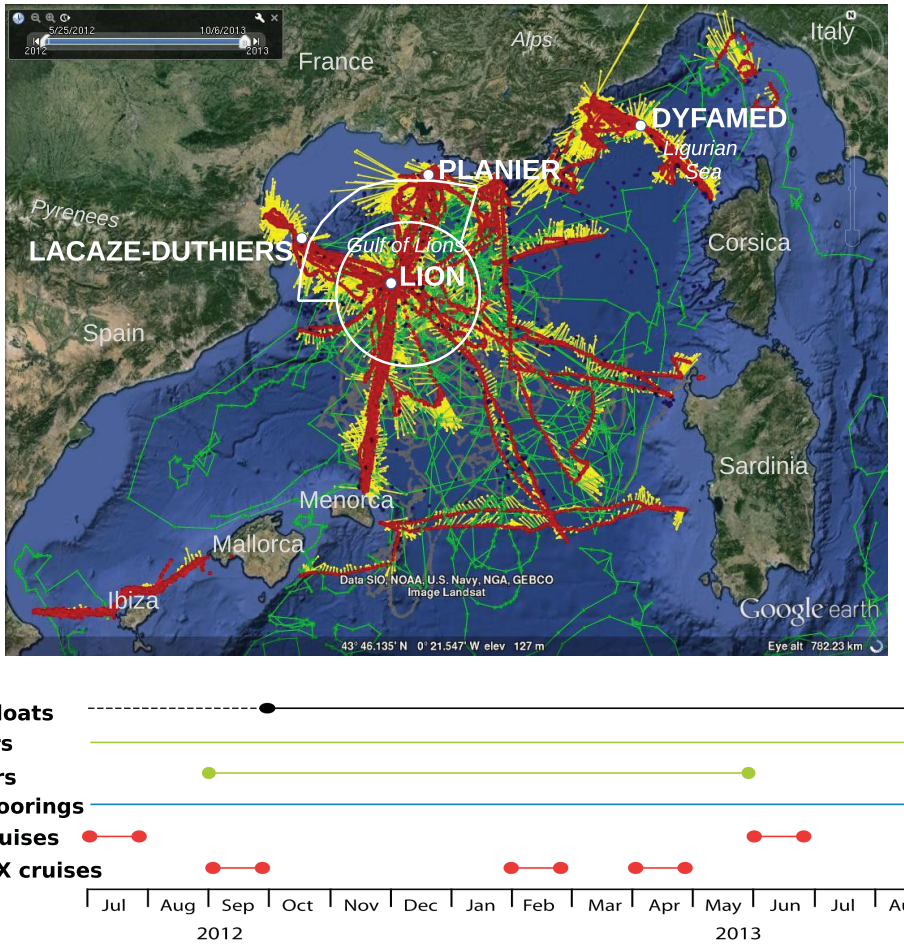

Figure 1. All observations carried out between 1 July 2012 and 1 October 2013. Gliders surface positions (red dots) and measured depth-average currents (yellow arrows). Profiling floats surface positions and trajectories (green). CTD casts from research cruises (blue). Surface drifters trajectories (grey). Positions of the LION, LACAZE-DUTHIERS, PLANIER, and DYFAMED moorings (white dots). The two selection areas "*Boundary Current*" and "*Mixed Patch*" used in Figure 4 are displayed in white.

network.fr) in this region, additional observations (Enhanced Observation Period, EOP and Special Observation Periods, SOPs) were carried out in the northwestern Mediterranean Sea to try to achieve the above mentioned goal, thanks to several European and national projects (see Acknowledgments). Thanks to numerous research cruises, gliders, profiling floats, moorings, and drifters, a very significant number of oceanic vertical profiles, could be collected to reach a better characterization of deep convection in this region, and the subsequent bloom.

The approach was to combine the sampling capabilities of R/Vs with autonomous platforms to reach an adequate spatiotemporal coverage during a period starting in Summer to the next, and to be able to capture all the key processes involved in deep convection during a year. Our "study period" was 1 July 2012 to 1 October 2013 and the data considered here includes gliders, ship CTD, profiling floats, drifters, and moorings. All data considered are displayed on Figure 1 together with the temporal sampling strategy for each platform.

Figure 2 describes typical ocean color satellite images that were obtained, when the sky was clear, and illustrates the different phases of deep convection. Summer-Fall is a period of low phytoplankton abundance followed by a Winter period during which high phytoplankton abundance can be observed around a "blue hole" in the deep convection area and then, a Spring period dominated by a planktonic bloom covering the entire northwestern basin until it fades away in late Spring.

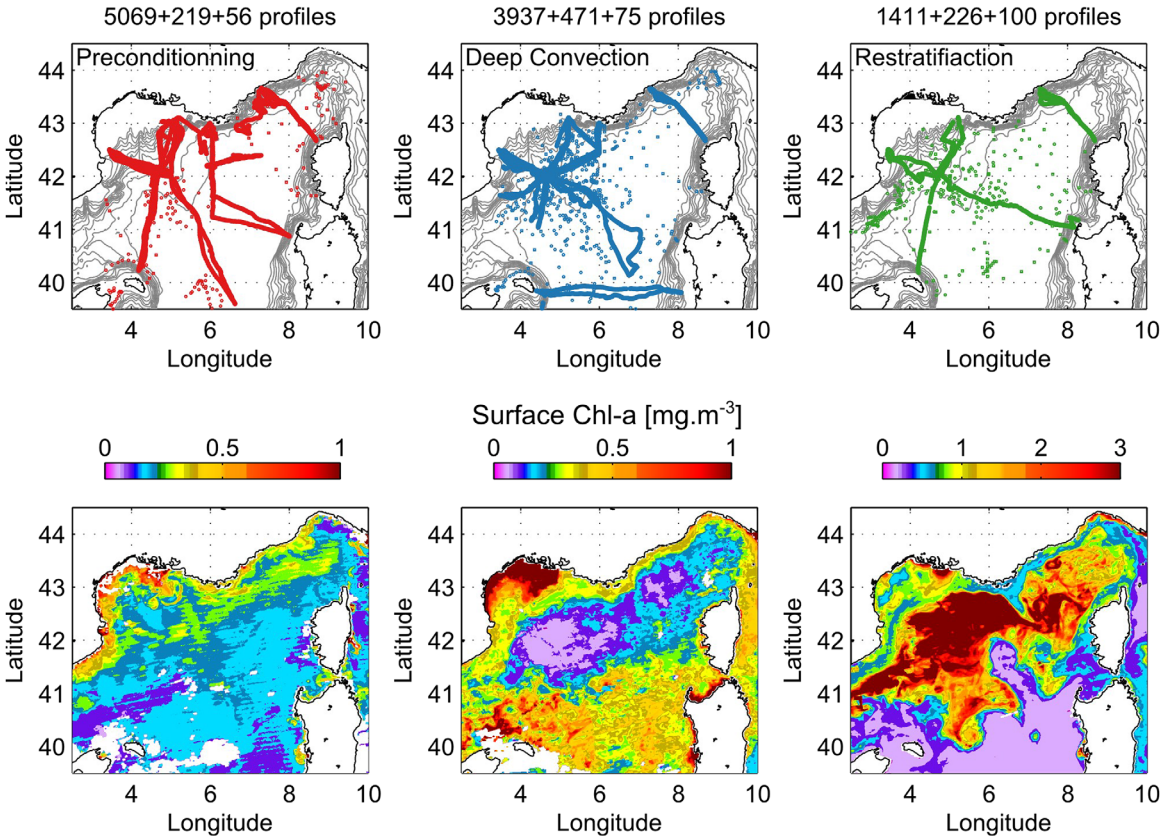

Figure 2. (top) Spatial coverage during the so-called "preconditioning" (1 September to 15 December 2012), "mixing" (15 December 2012 to 31 March 2013) and "restratification" (1 April to 31 May 2013) phases of deep convection. The number of profiles, respectively collected by gliders, Argo profiling floats and R/V is indicated. (bottom) Surface chlorophyll-a concentration retrieved by satellite (L3 MODIS product) and averaged on (left) 1–2 November 2012, (middle) 13–21 February 2013, (right) 12–14 April 2013 that correspond to cloud-free periods during each phase.

To really understand and assess the deep convection and bloom processes, a vertical description of the variations that can be observed with satellites was required and an optimal combination of the various in situ platform sampling capabilities has been sought. The observational efforts required:

1. periods of intensive observation at certain key moments (SOPs), allowing access to a full annual cycle for the entire zone. It is indeed essential to monitor the evolution of the ocean in the study area over specific periods of the year, so changes related to dense water formation can be assessed for both water balances and elements involved in the functioning of the ecosystem and the sequestration of matter;
2. a sampling strategy compatible with the large, mesoscale and submesoscale phenomena and which can be used effectively to constrain modeling studies.;
3. a coordination with periods of intensive atmospheric observations of intense events; and
4. a consistency with observations carried out on the long-term in the area.

Different models were used in this program in combination with the observational efforts presenting different configurations (and in particular horizontal resolution) depending on the different processes under focus (large/small space/time scales) and the sampling strategy was designed to provide validation (and initialization) at the subbasin scale as well as at submesoscale taking advantage of the different sampling capabilities of the platforms considered here.

Ship cruises were planned before, during, and after deep convection and bloom events, while gliders, profiling floats, moorings (at few locations), and drifters could provide information in-between. Even if this information is more limited in terms of observed variables, most of the autonomous platforms deployed during the study period were equipped with physical (temperature, salinity, currents) and bio-optical (dissolved

oxygen, chl-a fluorescence, turbidity, CDOM, nitrates) sensors and this allows a quasi-continuous description of the physical forcing on key biogeochemical variables.

Research cruises mainly intended to provide a CTD network covering the whole subbasin at different periods of the year. The CTD casts were mainly carried out at relatively low horizontal resolution (about 20 nm except on the continental slope where the distance between the CTD casts was lower in order to sample the boundary circulation) to cover the whole subbasin in about 3 weeks.

For gliders, the planned sections were designed with a low repeat rate but large spatial coverage before and after deep convection events, while repeat-sections at higher repeat rate (but smaller spatial coverage) were carried out during the "deep convection" period. During this period, the plan was to make the gliders turn back along their planned repeat sections as soon as the gliders were more than about 20 km away from the deep convection region.

Profiling floats were primarily deployed in the deep convection area just before, during, and just after the violent mixing events. The aim was to document the evolution of the *Mixed Patch* and to follow its break-up from a quasi-Lagrangian point of view, on even longer timescales.

Drifting buoys were deployed north of the deep convection area and in the deep convection area before, during, and after the violent mixing events. The aim was to document the surface temperature and salinity, and the atmospheric parameters during the period of strong surface heat loss.

One overarching objective with a massive deployment of autonomous platforms was to carry out about 40/300 profiles on average per day/week, distributed over the whole northwestern Mediterranean Sea, at any time during the whole deep convection/bloom period (including preconditioning and spreading/restratification phases) to adequately document the water column evolution.

3. Data

3.1. Ship CTD Data

Several, and often basin scale, cruises were carried out in the northwestern Mediterranean Sea during our study period (see Table 1). Since 2010, each of the MOOSE-GE cruise, on board *R/V Thetys II* or *R/V Le Suroît*, provides a yearly snapshot in summer of the open-ocean part of the basin with about 70–100 CTD stations distributed on a star-shape array centered on the deep convection zone with branches about perpendicular to the continental slope around. A major objective of the MOOSE observatory is to monitor the deep waters formation in the Gulf of Lions and to be able to detect and identify long-term environmental trends and anomalies of the marine environment and ecosystem in response to climate change. The remnants of the convective events happening in February are observed at the basin scale and this allows to monitor the deep water formation rate as for instance demonstrated by Waldman et al. (2016).

The DEWEX and DOWEX cruises, on board *R/V Le Suroît* and *R/V Tethys II* respectively, followed the same spatial sampling strategy and intended to cover the seasonal cycle with a focus first on the Winter-

Table 1
List of Cruises Carried Out in the Framework of the DEWEX Experiment

Cruises names	Ships	Dates	References
MOOSE-GE 2012	R/V Le Suroît	July 2012	Testor et al. (2012)
DOWEX 2012	R/V Tethys II	September 2012	Mortier (2012)
HyMeX SOP1	R/V Urania,	September 2012	Ducrocq et al. (2014)
	R/V Le Provence	October 2012	Taupier-Letage (2013)
DEWEX-1	R/V Le Suroît	February 2013	Testor (2013)
HyMeX SOP2	R/V Tethys II,	January,	Estournel et al. (2016a)
	R/V Le Provence	February,	Taupier-Letage and Bachelier (2013)
		March,	
		and May 2013	
DEWEX-2	R/V Le Suroît	April 2013	Conan (2013)
MOOSE-GE 2013	R/V Tethys II	June 2013	Testor et al. (2013)
DOWEX 2013	R/V Tethys II	September 2013	Mortier and Taillandier (2013)

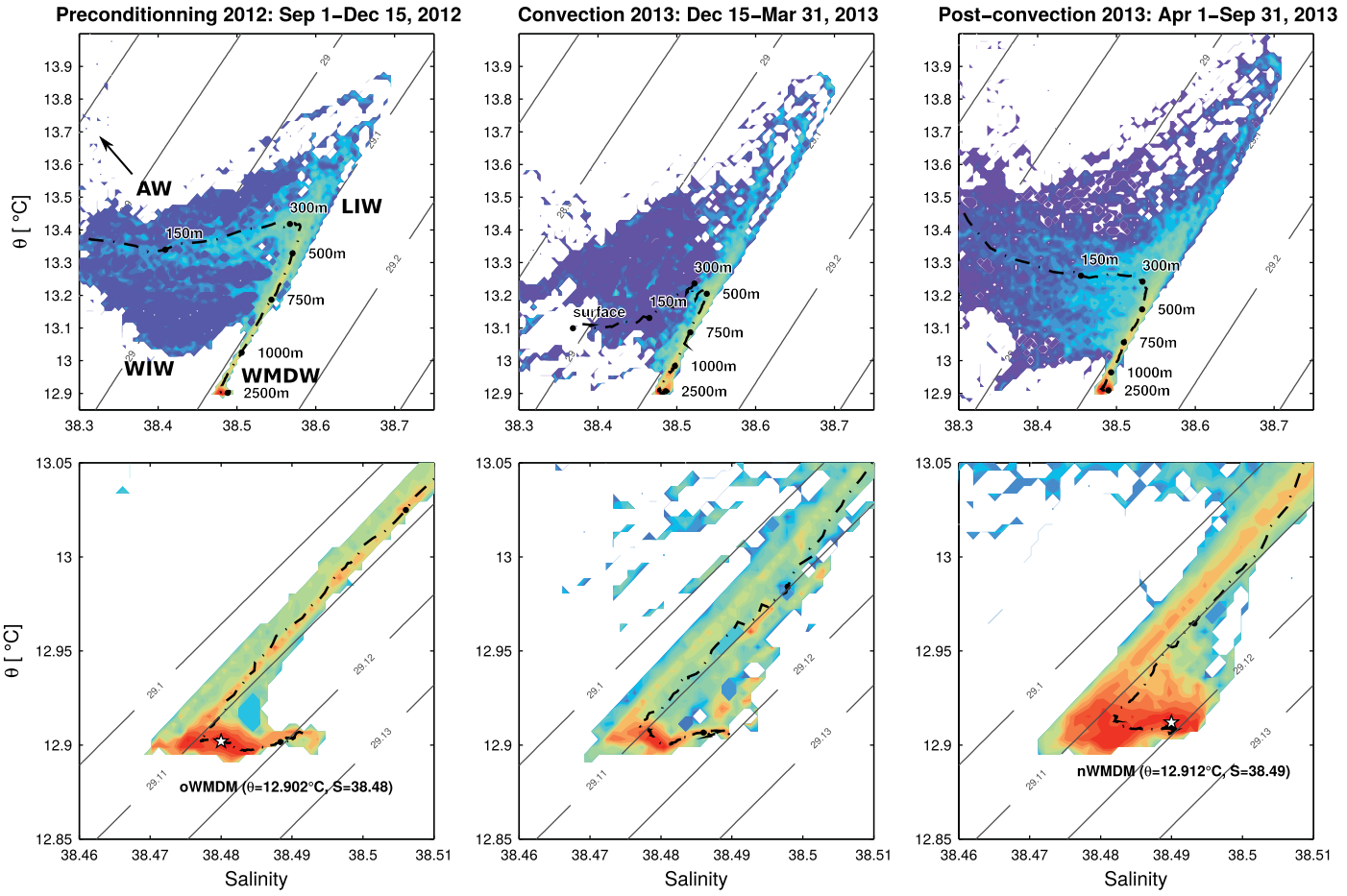

Figure 3. Probability density function in the θ/S space of all CTD casts data during the MOOSE-GE 2013, DOWEX 2012, HyMeX-SOP1 2012, HyMeX SOP2 2013, DEWEX 2013-1, DEWEX 2013-2, MOOSE-GE 2012, and DOWEX 2013 cruises, the 1% less frequent values being not shown. The dashed lines with depth labels represent the mean θ/S profile over each time period. The bottom plots focuses on the deep waters and shows the transformation of the deep waters during the convection event.

Spring period when deep convection and bloom occurs and second, in September for the preconditioning. They provided very accurate profile measurements every 20 nm or so, covering the whole basin. CTD casts have also been collected during the HyMeX SOP1 cruises (see Ducrocq et al., 2014; Lebeaupin-Brossier et al., 2014) from *R/V Urania* and *R/V Le Provence*, and during the HyMeX SOP2 cruises from *R/V Tethys II* and *R/V Le Provence*. To span the preconditioning period, Marisonde and Surface Velocity Program (SVP) drifters were launched from a dedicated cruise early September 2012, on a transect off Toulon (5°E). To deploy Argo floats in the Mixed Patch, and reposition the Marisonde buoys for the convection period, support cruises were set up late January and late February 2013. In order to catch an intense Mistral wind event and its impact on the convection, *R/V Le Provence* was chartered to enable sampling on alert (Estournel et al., 2016a). In total, about 400 CTD casts were carried out during our study period.

The ship CTD data are displayed on Figure 3. This is the reference data set and it describes well the different water masses that are present in the area during our study period. Because of the number of casts (among the highest numbers of CTD casts ever carried out in a year in this area), we certainly have a nice statistical description of all kind of profiles that can be observed, having in mind a water mass classification. One can identify the Atlantic Water (AW) characterized by a minimum in salinity and its modal form, the Winter Intermediate Water (WIW), the Levantine Intermediate Water (LIW) below, characterized by a maximum in salinity and in potential temperature, and the Western Mediterranean Deep Waters (WMDW) and the newly formed Western Mediterranean Deep Waters (nWMDW) generally at greater

depths, that are characterized by a potential temperature of 12.91–12.94°C and a salinity of 38.45–38.48, the highest values being typical of the newly formed waters and reciprocally, the lowest ones being typical of water formed previously. Figure 3a shows the profiles collected before the deep convection events with a narrow distribution around an almost linear relationship between the deep and intermediate waters. A white dot indicates the presence of nWMDW formed the previous year that cohabits with even older ones. During the winter mixing events (Figure 3b), the distribution of Θ-S values is more scattered (with lower probabilities) with a number of accumulation points often saltier than before. After a period of mixing, a significant volume of newly formed deep water emerges (around the white dot on Figure 3c). Note that this year, cascading was relatively weak compared to intense cascading events that can be observed every 6 years or so, as shown by Durrieu de Madron et al. (2013) or Houpert et al. (2016). Deep water formed by cascading apparently did not propagate very deep in 2012–2013. Such a water mass has been detected, as shown by glider sections crossing the continental shelf and slope along Cape Creus canyon and at the surface with the TRANSMED thermosalinometer (I. Taupier-Letage et al., personal communication, 2016), but is not visible on the Θ-S diagrams presented on Figure 3 and is not considered as a major newly formed deep water mass during this winter.

3.2. The Mooring Lines Data

The LION mooring line is in the vicinity of the center of the deep water formation zone at 42°02′N/4°41′E (bottom depth at 2,350 m, see Figure 1). It was equipped for the study period with 11 SeaBird Microcats SBE37 (conductivity-temperature-pressure sensor), 10 RBR temperature sensors, and 5 Nortek Aquadopp current meters measuring horizontal and vertical currents, spaced along the line from 150 to 2,300 m. The DYFAMED mooring line in the Ligurian Sea at 43°25′E/7°54′N was equipped similarly but with fewer instruments (four SeaBird Microcats SBE37 at about 200, 700, 1,000, and 2,000 m, Nortek Aquadopp current meters at 100 and 1,000 m). These moorings provide relatively profiles with low resolution along the vertical of the water column but about every 30 min, this rate being the lowest sampling rate of all instruments attached to the lines.

The LION and AZUR Météo-France moored buoys are located at about 42°06′N/4°38′E and 43°23′N/7°50′E close to LION and DYFAMED mooring lines, respectively. They provided hourly measurements of atmospheric parameters (atmospheric pressure, temperature, relative humidity, wind speed and direction, downward radiative fluxes) and surface oceanic parameters from a SeaBird Microcat SBE37 during our study period. Additionally, at the LION surface buoy, 20 NKE Instrumentation SP2T sensors provided hourly measurements of pressure and temperature from the surface down to 250 m to complement water column measurements carried out between 150 m and the bottom by the LION mooring line (Bouin & Rolland, 2011). Note that no surface turbulent heat (sensible and latent) and momentum flux measurement was carried out. Fluxes were estimated in this study from surface parameters through the use of turbulent flux parameterization from Fairall et al. (2003).

The LACAZE-DUTHIERS and PLANIER moorings, at about 42°25′N/3°32′E and 43°01′N/4°48′E respectively, were equipped with CTD sensors (Microcats) and current meters at 500 and 1,000 m depths. Like DYFAMED and LION/LIONCEAU (42°01′N/4°48′E), these two moorings are also equipped with sediment traps to monitor the fluxes through the canyons but only hydrographical data from these moorings are used in this study.

3.3. Profiling Floats Data

Profiling floats drift autonomously at a given parking depth for a given time period, typically 1–10 days. At the end of their drifting time, they dive to 2,000 m depth (or sometimes 1,000 m depth) and collect a profile of temperature and salinity during ascent to the surface. The collected data are sent in real-time to a data center before the floats return to their parking depth. During our study period, 27 floats deployed in the framework of Argo and MedArgo and Bio-ArgoMed, were active in this area. Due to the Mediterranean specificity, the MedArgo program has set the interval between the successive surfacing of Argo floats to be 4–5 days and their parking depth to ∼400 m, the approximate depth of the LIW. During our study period, other float configurations provided different results such as casts down to 1,000 m depth every day with parking depths at 1,000 m depth for some period of time or casts to 2,000 m depth every 5 days etc. For instance, bio-optical floats were configured to profile every day when drifting in the *Mixed Patch* to better observe it and then, when atmospheric fluxes reverted, were remotely

reconfigured to cycles of 5 days to document at a larger scale the spreading of the newly formed deep waters. Profiling floats collected a total of about 2,700 potential temperature and salinity profiles in the northwestern Mediterranean Sea during our study period. Many were equipped with oxygen sensors (Coppola et al., 2017) and others with nitrate, fluorescence of Chl-a, fluorescence of CDOM, and turbidity sensors (Mayot et al., 2017) to document the ventilation processes and the physical-biogeochemical interactions.

3.4. Drifter Data

Two types of drifting buoys were deployed during the HyMeX SOP1-SOP2 periods. SVP drifters provide measurements of atmospheric pressure, SST and SSS (SVP-BS type drifters) or water temperature from the surface down to 80 m (SVP-BTC drifters). They are attached to a 15 m drogue and follow the surface currents. Five salinity SVP drifters and five temperature SVP drifters were deployed before the deep convection period in the north of the Gulf of Lions. They provided a good coverage of the deep convection area before and during the mixing period. Marisonde buoys are particular drifters that measure the water temperature from the surface down to 250 m. In addition, they record atmospheric pressure, temperature, and wind. They are however more sensitive to the surface wind than to the current and cannot be considered as Lagrangian. Five of them were dropped in the north of the deep convection area at the beginning of September 2012, five more at the same place in February 2013 during the HyMeX SOP 1 and 2 cruises.

3.5. Gliders Data

Gliders (Testor et al., 2010) are steerable autonomous platforms that sample the ocean along saw-tooth trajectories between the surface and a maximum depth of 1,000 m today. As the slopes of isopycnals (a few degrees) are generally much smaller than the pitch angle of the glider (about $\pm$15–30°), the glider dives and ascents can be considered as vertical profiles to a large extent. Under this assumption, two consecutive profiles down to 1,000 m are separated by approximately 2–4 km and 2–4 h depending on the currents and the sampling strategy of the platform, with sensors being powered on during dives and/or ascents. With a horizontal speed of 30–40 km d^{-1} relative to the water, gliders are perfectly suited to capture balanced circulation features and eddies that propagate more slowly. By comparing dead reckoning navigation and GPS fixes at the surface, gliders can also deduce a depth-average current between two surfacing. The average of the currents over a dive provides a transport estimate, being close to a measure of the average currents between surfacing (generally 2–4 km apart) and between the surface and the depth achieved (generally 1,000 m depth). The gliders used during this experiment were equipped with the same sensors as for the profiling floats for measurements of potential temperature, salinity, but also oxygen concentration, fluorescence of Chl-a, fluorescence of CDOM, and turbidity. They provided about 40,000 profiles over our study period.

4. Data Harmonization and Integration

4.1. Temperature and Salinity Estimates

Two coupled Seabird SBE 911+ CTD were used during MOOSE-GE/DOWEX/DEWEX cruises with pre and postcalibrations from the manufacturer. The data have also been compared to the analysis of the Rosette water samples with a Guideline Autosal. The absolute accuracy of this calibration method is estimated to be about 0.005 for the salinity, and 0.001°C for the temperature. These calibrated CTD casts provide a ground truth used for the calibration of other instruments such as the deep mooring lines (LION and DYFAMED in particular) and the data collected by autonomous gliders, profiling floats through alignments on a linear T/S relationship observed at depths (700–1,000 m) each year at the basin scale, and point-to-point intercomparison exercises.

An intercalibration of the instruments on the LION and DYFAMED mooring lines after and before each deployment has been carried out to ensure the consistency of the mooring sensors with the ship CTD data set. Each year, during the mooring maintenance operations, microcats are attached to the Rosette and a cast consisting in a 20 min stop at 1,000 m depth is carried out with all the instruments. A relative calibration of the moored instruments with each other and relative to the shipborne CTD probe SBE 911+ is performed as in Testor et al. (2016).

Each glider is equipped with a pumped or unpumped CTD sensor that generally needs to be corrected with an offset as a first-order correction for each deployment. By comparing the gliders data in the deep layers (700–1,000 m) with nearby calibrated CTD casts collected by R/V ($<$15 km and $<$3 days), and/or with the calibrated data of the mooring lines LION and DYFAMED ($<$2.5 km and $<$18 h, about the inertial period in this region), we checked the consistencies of the hydrographical data in the deeper layers sampled by the gliders, as the variability of the temperature and salinity are relatively small at those depths (Bosse et al., 2015, 2016). The deduced offsets that are applied are on average of about 0.01°C and 0.01 in Potential Temperature and Salinity, respectively. In addition, the method of Garau et al. (2011) was used to correct thermal lag issues of the gliders pumped and unpumped CTD probes. Note this applies second-order corrections everywhere but in sharp summer thermoclines (order of 1–10°C over less than 10 m) where salinity measurements can indeed be affected. If no direct comparison with calibrated data is possible ($\sim$30% of the deployments), only salinity is offset to fit the linear θ–S relationship holding between the intermediate and deep layers (700–1,000 m) and provided by the calibrated data from R/V (see Figure 3). Glider time series have been sliced in up and down casts and interpolated every 1 m along the vertical to provide equivalents of vertical profiles located at average up or down casts times and locations.

We applied similar calibration procedures for the Argo profiling floats and drifters equipped with thermistor chains below, as for the gliders. The thermal lag issue is a known problem for profiling floats too (gliders are equipped with the same probes) but when vertical resolution is not high enough to resolve the thermocline (and this is often the case for profiling floats not configured to resolve sharp thermoclines), no thermal lag correction could be applied and a vertical interpolation just applied. No correction was applied on drifters thermistor chain data, time series data being just interpolated along the vertical on a 1 m basis, like mooring data, to estimate profiles.

This method ensures the autonomous platforms CTD errors in temperature and salinity to overall be smaller than, respectively, 0.01°C and 0.01. On the other hand, the variability in θ-S characteristics could be estimated with unique platforms at different levels based on a water mass identification approach. As illustrated by Figure 4f, differences between the nWMDW in 2013 and former WMDW at great depth are about 0.04°C in potential temperature (and 0.03 in salinity, not shown). Similarly, the differences in potential temperature and salinity between nWMDW and LIW (maxima of Potential Temperature and Salinity) are about 0.3°C (Figure 4e) and 0.3, respectively, in the intermediate layers. Finally, the differences between nWMDW and AW (minimum of Salinity) are about 0.4 in salinity with a wide range of relatively similar temperatures at any time (prominence of the seasonal cycle) in the open sea region (Figure 4d). Therefore the overall corrected data set can be considered as consistent in accuracy for studying the evolution of the water masses and the deep convection processes, with a reference to high-quality values from ship measurements and water samples.

4.2. Chl-a Concentration Estimates

During MOOSE-GE, DOWEX, and DEWEX cruises, Chlorophyll-a fluorometers calibrated by manufacturers were available on all kind of platforms (i.e., ships, gliders, profiling floats). Moreover, water samples were filtered during ship surveys to estimate Chlorophyll-a concentration through High Pressure Liquid Chromatography (HPLC) technique (Gieskes & Kraay, 1983). The harmonization of the whole fluorescence data set was carried out by using the Lavigne et al. (2012) technique, which provides fluorometer-specific calibration coefficients (offset and slope) by comparison with ocean color satellite images. Briefly (see Lavigne et al., 2012 for a complete explanation of the method), fluorescence profiles are initially corrected for photochemical quenching (Xing et al., 2012); then an offset is evaluated by imposing zero value at depth below the Mixed Layer. Satellite match-ups were then generated (+/– 4 h temporal difference with satellite overpass, using daily MODIS level 3, at 4 km spatial resolution products) and used to calculate slope coefficients. Slope and offset coefficients were first evaluated on a single profile basis. Then, to keep the high spatiotemporal variability measured by autonomous platforms, a single coefficient was defined for each platform (for floats), for each deployment (for gliders), or for each leg (for ships), by using median values. A visual check of the time-series of the slope and off-set coefficients allowed to verify there was no significant drift in fluorometer during float or glider missions or ship legs. When available (i.e., for most of the ship fluorescence profiles, and on some autonomous platforms), a direct comparison of the satellite-calibrated fluorescence with HPLC Chlorophyll estimations was carried out (not shown). The median error is of 28%, indicating a general good performance of the harmonization method applied here. Note that an enhanced calibration

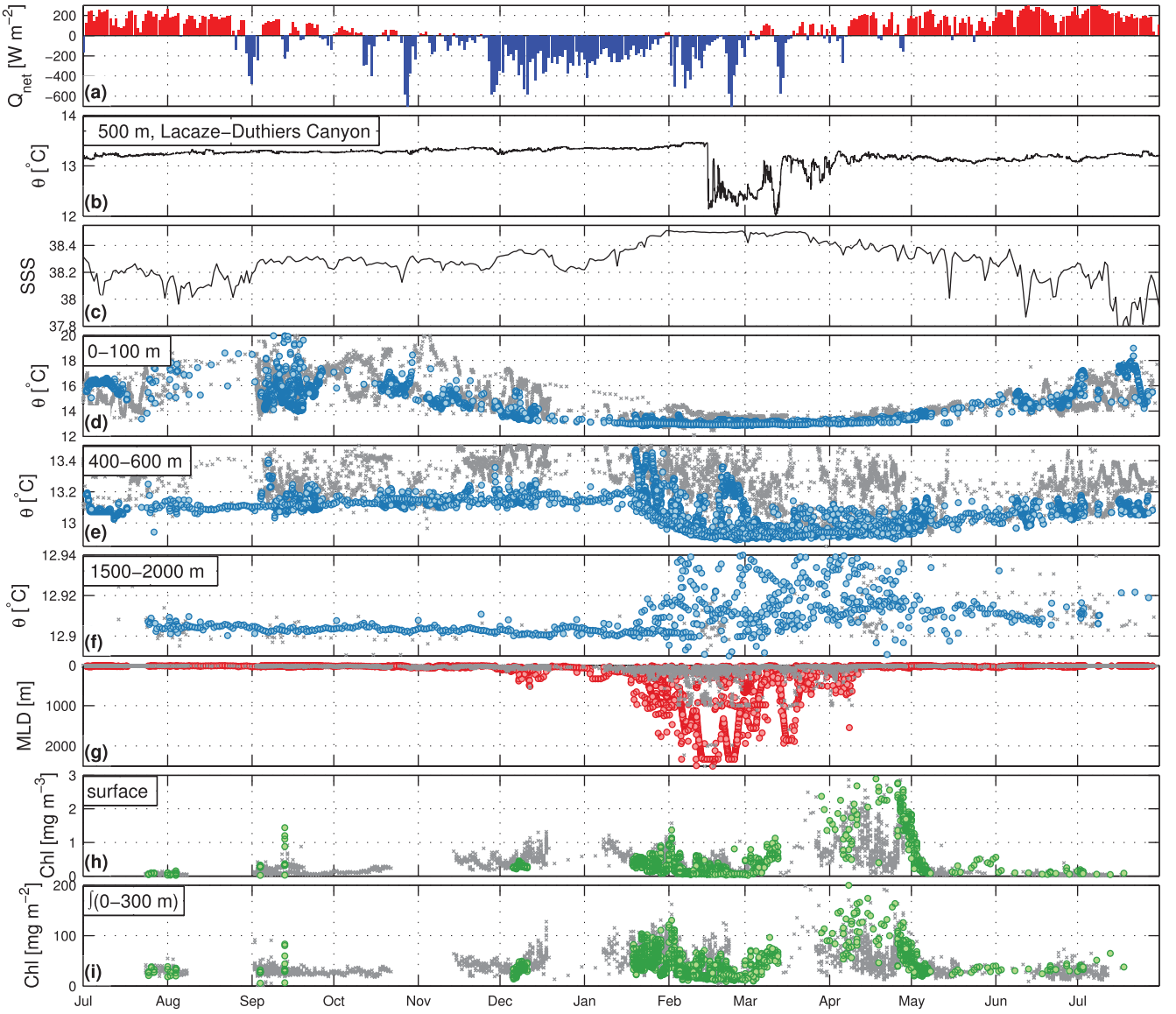

Figure 4. Time series of: (a) estimated net heat fluxes at the LION buoy; (b) potential temperature at 500 m recorded in Lacaze-Duthiers canyon (Gulf of Lions shelf); (c) sea surface salinity at the LION buoy; (d) potential temperature average over the layer 0–100 m; (e) potential temperature averaged over the layer 400–600 m; (f) potential temperature average over the layer 1,500–2,000 m; (g) Mixed Layer Depth (MLD) estimates as in Houpert et al. (2016); (h) estimates of chl-a at surface; and (i) estimates of chl-a integrated over 0–300 m. Light colors correspond to the "*Boundary Current*" selection area while darker colors correspond to the "*Mixed Patch*" one (see white delineated areas on Figure 1).

of the available fluorometers was provided by Mayot et al. (2017), who opted for an improved calibration (by directly comparing fluorometers data with HPLC), although a degraded data availability (only floats and ships having simultaneous HPLC samples at the float deployment or during the ship surveys were used). Margirier et al. (2017) demonstrated, however, that the satellite-derived calibration presented here is only slightly less accurate than their enhanced method.

4.3. Depth-Average Current Estimates

Calibrations of the compasses of the gliders have been performed before each deployment. The current estimates were corrected using estimates of the angle of attack from the flight model used in Margirier et al. (2017) Indeed, the typical angle of attack of a glider is about 3° (during dives and opposite during ascents) and induces an artificial forward oceanic current in the depth-average current estimates, if not

taken into account. When possible, the depth-average current estimates from gliders where compared to the mooring current meters data (at 150 and 1,000 m data) and the data were consistent for 1 cm s^{-1} when all mooring current meters data were strongly correlated and somewhat representative of the 0–1,000 m water column. Return points along trajectories allowed comparisons of depth-average current estimates within few hours and kilometers. Such a protocol ensures a relative accuracy of about 1 cm s^{-1} for both components of the estimates of the depth-average currents, typically about the expected natural variability of depth-average currents over such scales. This allows discarding the few data clearly having a compass bias over a whole glider deployment (no deployment was discarded during our study period, but considering older data, it looks it is a quality control to apply). Outliers ($>$ 1 m s^{-1}) certainly due to spurious and bad GPS fixes correspond to 0.1% of the data and were discarded from our data set. In this study, we consider only 1,000 m depth-average currents. This includes currents in the open sea but also part of the boundary circulation which flows roughly centered above the 1,000 m isobath. It excludes depth-average current estimates over shallower dives which are not directly comparable to depth-average current estimates over 0–1,000 m. The currents are generally more intense at the surface than at great depth and depth-average currents estimated over shallower dives reflect the baroclinic component in a different way. Keeping only depth-average currents estimates over 0–1,000 m allows having a consistent data set for currents averaged along the vertical over this layer.

5. Objective Analysis

Our objective analysis method consists in extrapolation in 2-D along the horizontal from several point observations distributed in space and time using a correlation function (Le Traon, 1990). At first order, one can consider a Gaussian correlation function describing fluctuations at given spatial and/or temporal scales L: $Cov(a,b)=E+Se^{-D(a,b)^2/L^2}$, $D(a, b)$ being the temporal/spatial distance between two observations "a" and "b." S/E is the signal over noise ratio. The error is considered small, about 10% of the estimated variance of the signal.

To take into account the tendency of oceanic currents to follow f/H, f being the planetary vorticity and H the bottom depth, we can introduce an anisotropy as described in Boehme and Send (2005). The covariance function considered is then: $Cov(a,b)=E+Se^{-D(a,b)^2/L^2-F(a,b)^2/\Phi^2}$, $D(a, b)$ and $t(a, b)$ is the spatial distance, $F(a, b)$ is a distance in potential vorticity f/H defined as: $F(a,b)=|Q(a)-Q(b)|/\sqrt{Q(a^2)+Q(b)^2}$ with $Q=f/H$. By taking $\Phi \simeq 0.1$, the ocean is relatively isotropic except in the continental slope areas where the data are clearly more correlated along-shore than cross-shore.

For a considered data set, these methods are used with respect to a large scale first guess constructed with all data collected over the seasonal cycle. The data are first binned on a grid of 10 km $\times$ 10 km on a monthly basis and then analyzed with a scale $L = 150$ km corresponding to the basin-scale gradients and relatively high errors of 70%. Then two further refinement steps are preceded. The first consists in an analysis at the mixed patch scale ($L = 75$ km) with the observations carried out in a $\pm$10 days period with a relative error of 60% in order to capture the large scale and intraseasonal evolution of the mixed patch. Then a second step is performed using a smaller decorrelation scales ($L = 15$ km) and a smaller error of 10% in order to capture the mesoscale variability of the deep convection area. An analysis could be done every 10 days from January to March at the basin-scale with a good data coverage thanks to the intense observational effort during that period. Analyses were performed for potential temperature, salinity, potential density, and chl-a estimates over the whole domain with respect to related first guesses and the method provides geometrical error maps.

6. Results

6.1. Evolution of the Deep Convection Area

Figure 4a shows time series of total heat fluxes characterized by a series of storm events starting in September with important heat losses from the ocean about 400–800 W/m^2. The heat fluxes are consistently negative starting in November inducing a clear decrease in surface temperature (Figure 4d) but no clear signal in surface salinity except in February during which the salinity reaches a plateau of relatively high values (Figure 4c). The cascading mentioned above can be observed on Figure 4b but it happens mid-February

after the mixing has reached the bottom offshore (Figure 4g) and there is no signature at 1,000 m at Lacaze-Duthiers mooring (not shown).

Different time series of potential temperature from in situ profile data are also shown in Figures 4d, 4e, and 4f, describing well the evolution of the deep convection area over the water column, with respect to the boundary current region where advection dominates (time series in grey).

Figures 4d and 4e show the evolution of the surface and intermediate waters, respectively. There is always a contrast in the potential temperature between the convection area and the boundary currents where water masses are advected and less modified by vertical mixing processes. They also show the vertical propagation of the mixing, the temperature averaged over the deepest layer reaching progressively the same values as above.

The Mixed Layer Depth (MLD) was estimated with the method of Houpert et al. (2016) (see Figure 4g). These estimates show a slow deepening starting in October and a rapid one starting late January (at about 1,000 m depth) before the mixing reaches the bottom (mid-February) and this is consistent with the time series of temperature above. It also shows a period of deep mixing from the beginning to the end of February with a rapid restratification at the beginning of March. The heat fluxes (see Figure 4a) are positive for a short period of time before a second deep convection event triggered by a storm mid-March. Deep convection reached the bottom again at that time. This second mixing event is quite frequent when ones consider the deep convection from one year to another (Houpert, 2013). The short period of restratification allows to have very few buoyant waters on-top of homogeneous ones and such stratification is easily eroded by a storm during this period.

Changes in potential temperature in the deeper layers (see Figure 4f) occur at the beginning of February. A CTD cast performed few hours after a storm confirmed the winter mixing has reached the bottom by mid-February 2013. It raises sharply from 12.9 to 12.94 and then significant variations due to the presence of both WMDW and nWMDW in the area converge slowly to 12.91 at the beginning of May. At this stage old and newly formed WMDW are relatively well-mixed in the convection area and the variability returns to a low level, similar as before the rapid rise, but a large volume of water has increased in temperature and this corresponds to a significant heat storage.

The time series on Figures 4h and 4i illustrate how the phytoplankton responds to the environment. The amount of estimated chl-a at the surface and on average seems to increase mid-December when the MLD starts to present values greater than the base of the euphotic layer at about 100 m depth. At that time the winter mixing reaches waters that are nutrient-rich and nutrients being brought to enlighten levels, this participates to the growth of phytoplankton as shown in D'Ortenzio et al. (2014); Pasqueron de Fommervault et al. (2015). When the mixing reaches depths greater than 1,000 m, the surface chl-a drops to lower values before a sharp increase mid-March during the restratification period. It is likely the surface chl-a has dropped to low values again during the second deep mixing event mid-March but unfortunately, very few platforms considered here were equipped with a fluorometer at that time. However, enlarging the spatial domain (as in Mayot et al., 2017) the effects of the second event on the chlorophyll distribution could be monitored. Surface chl-a values reach even greater values in April before a rapid decrease in May once the system has stabilized and the nutrients have been consumed in the euphotic layer.

It is interesting to note that the low surface chl-a values observed before the restratification may result from dilution as the average chl-a over 0–300 m (Figure 4i) presents significant values of integrated chl-a compared to what can be estimated from the surface only. In terms of productivity, the integrated chl-a concentration (reaching about 100 $mg.m^{-2}$) is about the same during the slow deepening of the mixed layer, the deep convection violent events, or the planktonic bloom. The continuous (but slow) introduction of nutrients in the surface (mixed) layer during the fall contrasts with the rapid and massive introduction of nutrients just after the deep mixing events. Mayot et al. (2017) concluded that the spring bloom is more important than the autumnal one because of a dilution effect during the mixed layer deepening. They concluded the higher net accumulation rate of phytoplankton in spring in this region was not induced by a higher winter replenishment of nitrate. The strong and long winter mixing could rather have induced a change in zooplankton grazing pressure and silicate availability, leading to a stronger phytoplankton spring bloom. Furthermore, a similar autumnal phytoplankton bloom (less intense than the spring bloom) between bioregions might be ascribed to a mixing of the summer deep chlorophyll maximum, to inputs of nutrients in the surface layer, and/or also to photoacclimation processes.

6.2. Energy Fluxes

Thanks to the depth-average currents measured by the gliders, the evolution of the energy content of the basin can also be described. Due to deep convection, newly formed deep waters form a volume of water denser than the surroundings. This increases the potential energy of the system and is an energy reservoir that is then transformed into kinetic energy, through baroclinic instability as demonstrated by Gascard (1978); Legg and Marshall (1993); and Visbeck et al. (1996). During the restratification phase, very high currents, mainly barotropic, order of 30–40 cm s^{-1} can be observed at LION (Houpert et al., 2016). This is consistent with the expected results of baroclinic instability with a transfer of Available Potential Energy (APE, here considered as proportional to the integral of potential density profiles) into Kinetic Energy (KE) and a barotropization of the currents. The kinetic energy (KE) could be estimated from the depth-average currents (average over 0–1,000 m only) and the kinetic energy due to the fluctuations of the currents, the Eddy Kinetic Energy (EKE), by considering those depth-average currents minus a large-scale depth-average current, low-pass filtered with a scale of 100 km along the glider trajectories (Figure 5).

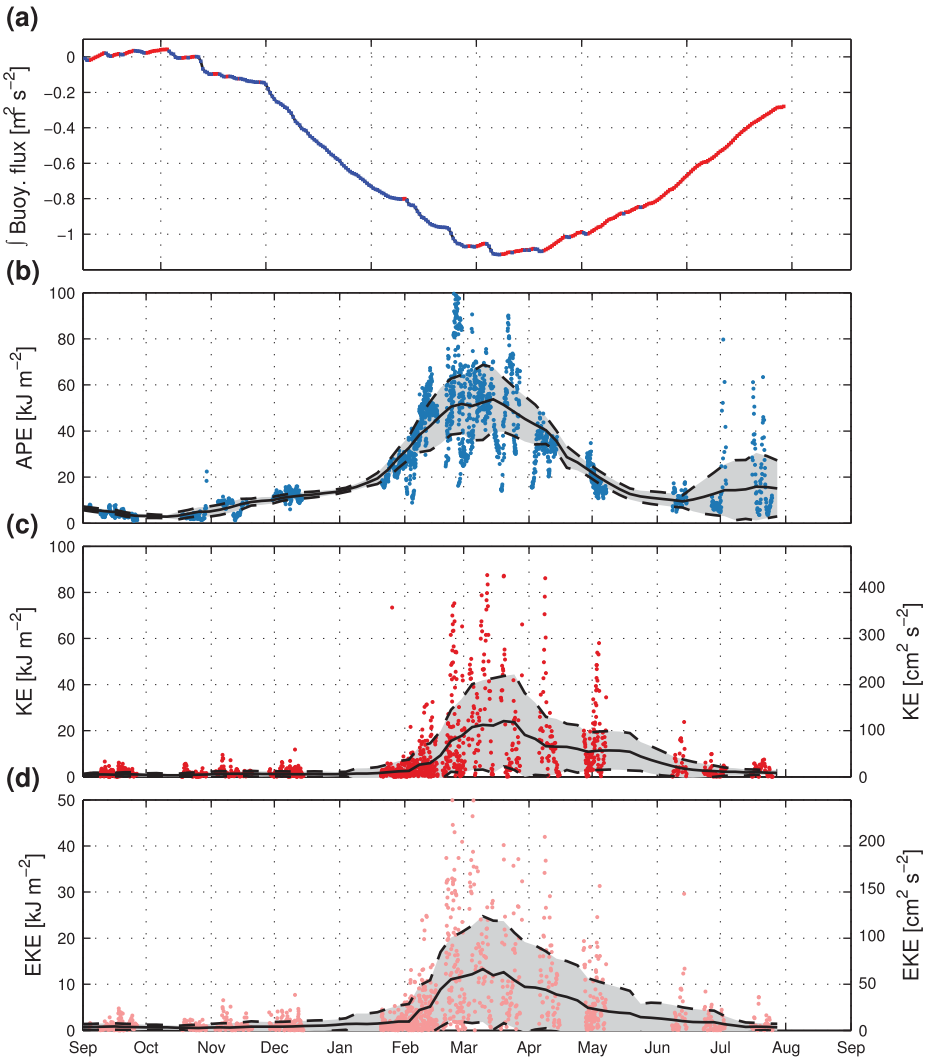

Figure 5. Time series of: (a) integrated buoyancy flux estimated at the LION meteorological buoy (blue dots indicate negative net heat flux, and red positive ones); (b) Available Potential Energy (APE) integrated from the surface down to 1,000 m from all glider density profiles; (c) total Kinetic Energy (KE); and (d) Eddy Kinetic Energy (EKE) estimated for 0–1,000 m layer from the glider depth-average currents. The black line shows the mean signal binned into 5 days period and smoothed with a moving average of 30 days. The gray-shaded area represents the standard deviation in each 5 days bin.

Noteworthy, the KE and EKE start to increase late January–early February when the mixing reaches depths of about 1,000 m (see Figure 4g). At this stage, the conversion of potential into kinetic energy starts and this will increase until the system reaches a maximum in potential energy. This clearly illustrates the violent mixing phase and the spreading overlap. The maximum in potential energy is reached by early March. At this stage, the heat fluxes at the surface are not able to extract sufficient buoyancy to overcome lateral fluxes due to eddies. The maximum in EKE is reached about 2 weeks later and this gives evidence to a response time scale for the development of instabilities resulting in the break-up of the *Mixed Patch*. About half of the increase in KE is due to eddies while the other half due to larger-scale currents (the Northern Current and the recirculation associated to the North Balearic Front south of the convection area). Deep convection is thus associated with an increase in intensity of these large-scale circulation features. This can be due to a large-scale response to the intensification of the lateral gradients of density as the water column gets denser and denser through deep convection processes in the *Mixed Patch*.

The nonfiltered data in APE show large variations with a first peak mid-February when deep convection first reached the bottom followed by scattered high and low values. One can observe the same pattern again mid-March during and after the second deep convection event. This illustrates the homogenization of the area during the deep mixing events, while the area is characterized by both mixed profiles (high APE) and stratified ones (lower APE). High values of nonfiltered KE and EKE can be observed at the same times but also later on, until the APE, KE, and EKE reach low values again.

6.3. Spatiotemporal Coverage and Budgets Estimates

Figure 6 shows analyses of MLD, averaged salinity over the surface layer (0–100 m), averaged potential temperature over the intermediate layer (400–600 m), and average chl-a profiles over the 0–300 m. Data are considered on the 10 km $\times$ 10 km grid over periods of 1 month with respect to the related first guess. Extrapolated values being estimated to have an error of more than 95% (in terms of variance) based on the 75 km analysis are shaded. It shows that the amount of collected information provides a convenient spatiotemporal coverage and allows to describe the deep convection process on a continuous basis at various scales throughout the year.

Figure 6c shows there is a maximum salinity expression in the surface layers and Figure 6b minimum potential temperature expression at intermediate depths on the analyses of 14 February concomitant with deep mixed layers ($>$ 1,000 m). Winter mixing actually transforms into deep convection at that time, once the winter mixing has eroded the LIW layer. Then, the signal fades away, more quickly in the surface layers. Figure 6d presents analyses of chl-a estimates averaged over 0–300 m and it is consistent with Figures 4h and 4i. The development of the phytoplankton starts in the deep convection area as early as September when the MLD starts to deepen. Later on, in February, phytoplankton seems to develop around the *Mixed Patch* before the bloom in April. In April, chl-a estimates present high values at the scale of the basin, from the Gulf of Lions to the Ligurian Sea, and even higher values in the deep convection area. Then, phytoplankton disappears rapidly with very low values everywhere in June.

The very large number of in situ observations harvested between January and May allows to solve in a quasi-synoptic way the typical scales of deep convection, and the same methodology was applied at a higher frequency. Figures 7 and 8 show high-frequency (10 days) analyses of the MLD and potential density at 1,000 m depth, respectively, with the related first guess being the previously described (monthly) analyses.

MLDs greater than 1,000 m depth can be observed starting in mid-January in the western part of the Gulf of Lion and the surface of the *Mixed Patch* increases until the beginning of March reaching a maximum extent of $28 \pm 3\ 10^9 m^2$ late February. It then quickly restratifies. The analyzed fields are sometimes patchy at the small scale but the general evolution emerges well with a break-up starting late March. The deep mixing occurs at the end of January with the formation of dense waters ($>$ 29.11 kg m^{-3}). The density of the newly formed waters increases after it has reached the bottom early February. The newly formed deep waters are characterized at that time by a density anomaly of about 0.01 kg m^{-3} and this remains identifiable in the months that follow—in particular in April, with a slow and general movement toward south and west. The amplitude of the density anomaly decreases throughout the restratification processes until May, with a progressive flattening of the isopycnals at the basin scale. These analyzed fields are consistent with

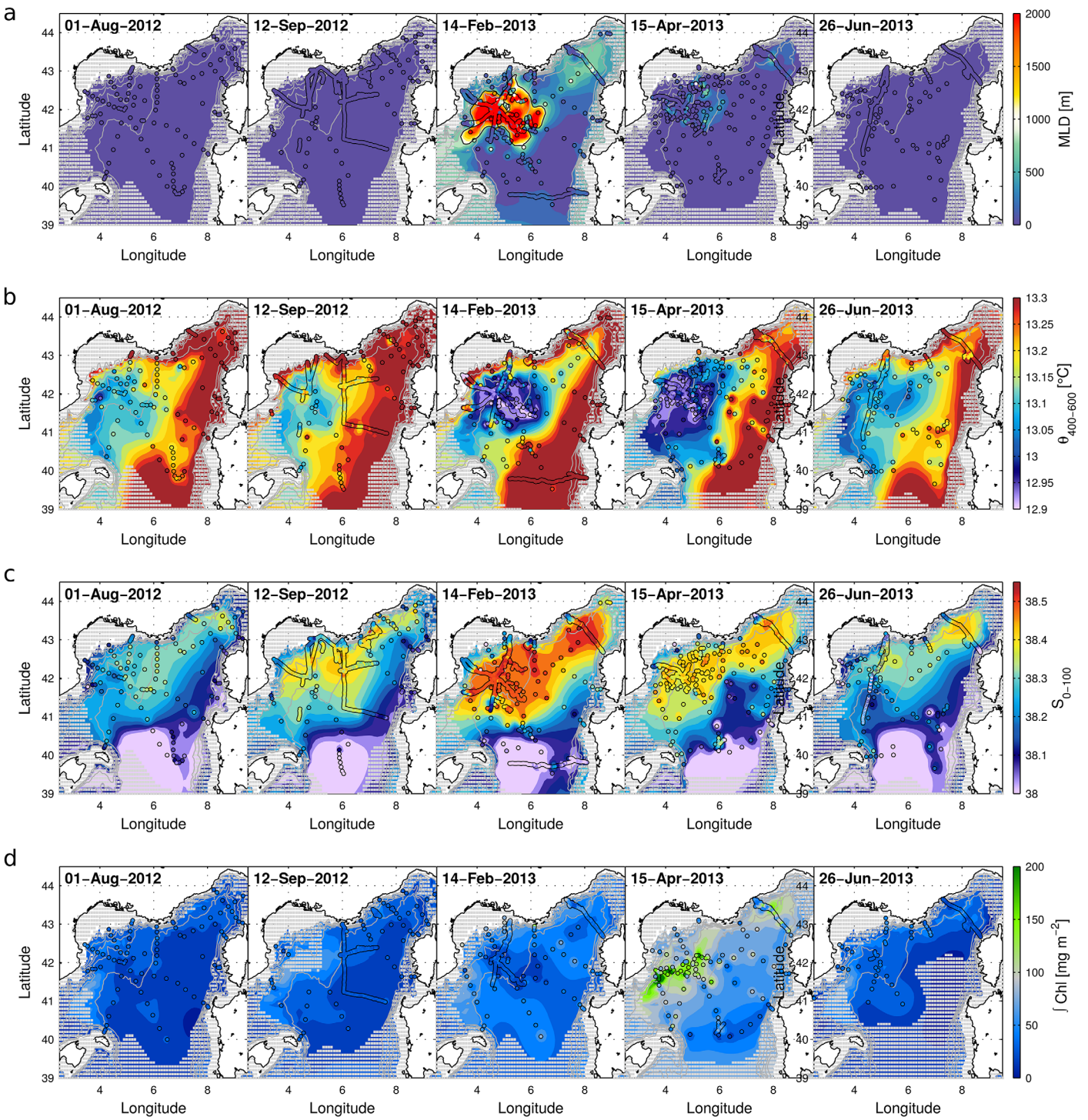

Figure 6. Objective analyses of (a) MLD estimates as in (Houpert et al., 2016), homogeneous profiles over more than 1,000 m were extrapolated to the bottom along the vertical thanks to LION mooring data (b) surface salinity (averaged over 0–100 m), (c) potential temperature at intermediate depth (averaged over 400–600 m), (d) chl-a estimates averaged over 0–300 m. Extrapolated values being estimated to have an error of more than 95% in terms of variance of the analyzed field at 75km are shaded. Data points within ± 10 days from the date of the analysis are superimposed (thin black circles filled with colors coded with values).

the time series of Figure 4 and describe the evolution of the area, with a lower time resolution but a description of the spatial patterns associated with deep convection.

The 4-D analysis in space and time of the density field in particular, allows us to analyze the transformations of the water masses that take place within the deep convection area. Figure 9a shows the evolution of the

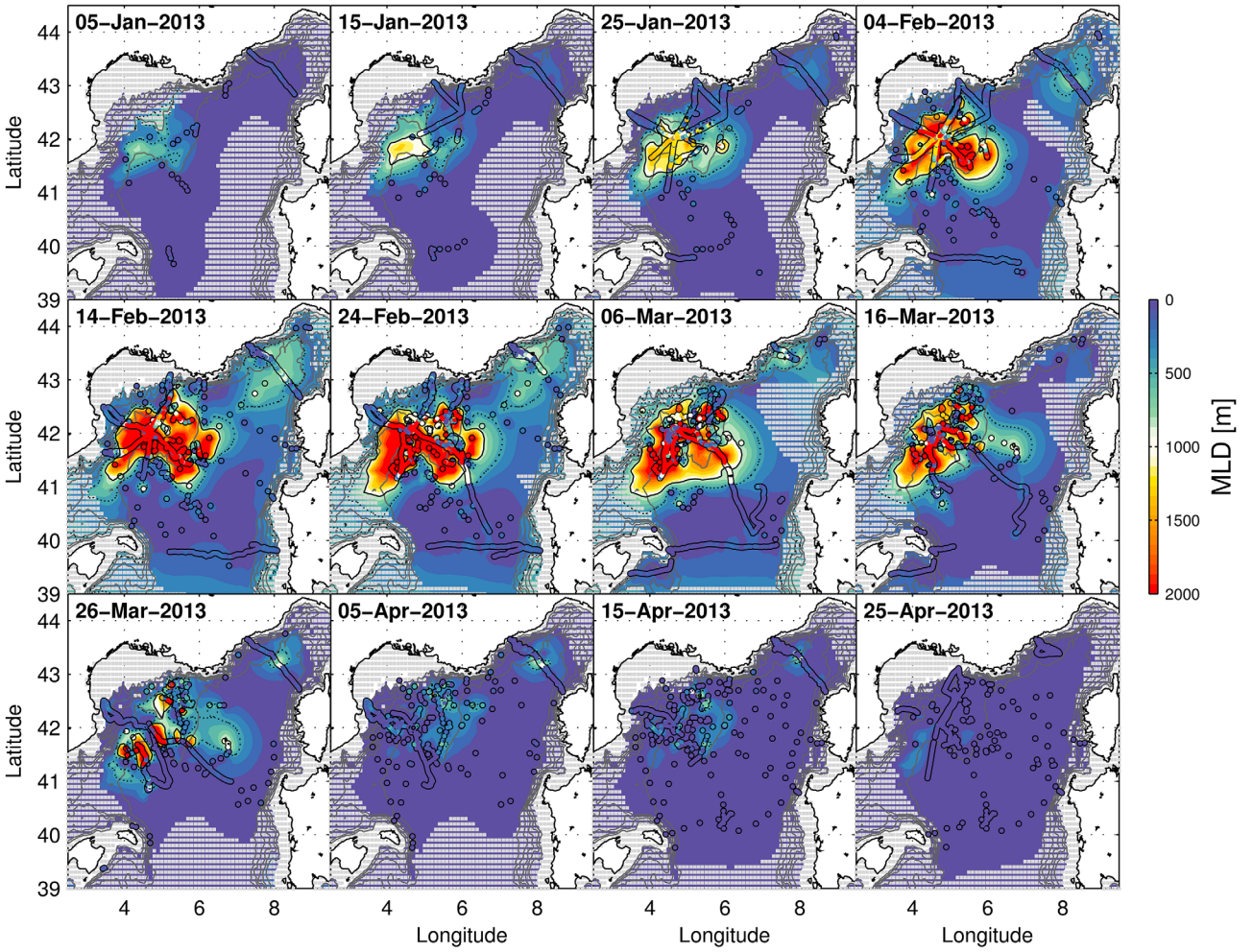

Figure 7. Objective analysis of MLD similar as in Figure 6 computed on a 10 day basis. Continuous and dashed black contours indicate MLD greater than 1,000 and 500 m, respectively.

volume of water denser than certain selected potential density thresholds, between mid-January and May. These estimates have been made over a relatively large area but restricted to the box as displayed on Figure 8, for a good coverage. The total volume of water presenting potential densities > 28.00 kg m^{-3} (σ_0) in the area under consideration is relatively constant over time, with a volume of 1.6×10^5 km^3, the volume under consideration being in fact composed quasi-totally by waters denser than > 28.30 kg m^{-3}. The time series associated to denser waters volumes present increases, the denser the later, as a result of transfers between the different isopycnal layers.

The relatively light waters presenting potential densities < 29.11 kg m^{-3} are progressively transformed into denser and denser waters during the violent mixing events starting mid-January for waters presenting potential densities > 29.11 and < 29.115 kg m^{-3}, and later on with the apparition of new waters presenting potential densities > 29.115 and < 29.12 kg m^{-3} early in February, and even denser new waters (> 29.12 kg m^{-3}) mid-February. During restratification periods, the opposite effect is observed: the volumes of dense waters decreases, while they spread out of the area of the Gulf of Lions, mix with other waters (with transfers from density classes to others) and light waters reinvest it.

The increase in volume is generally rapid for the different classes of water > 29.11 kg m^{-3} and followed by a general decrease. The fact that all these time series decay at about the same rate denotes a general input of lighter waters that can be better observed on Figure 9b as the volume (averaged over a year and expressed in Sv in order to be compared with other numbers that can be found in the literature) increases

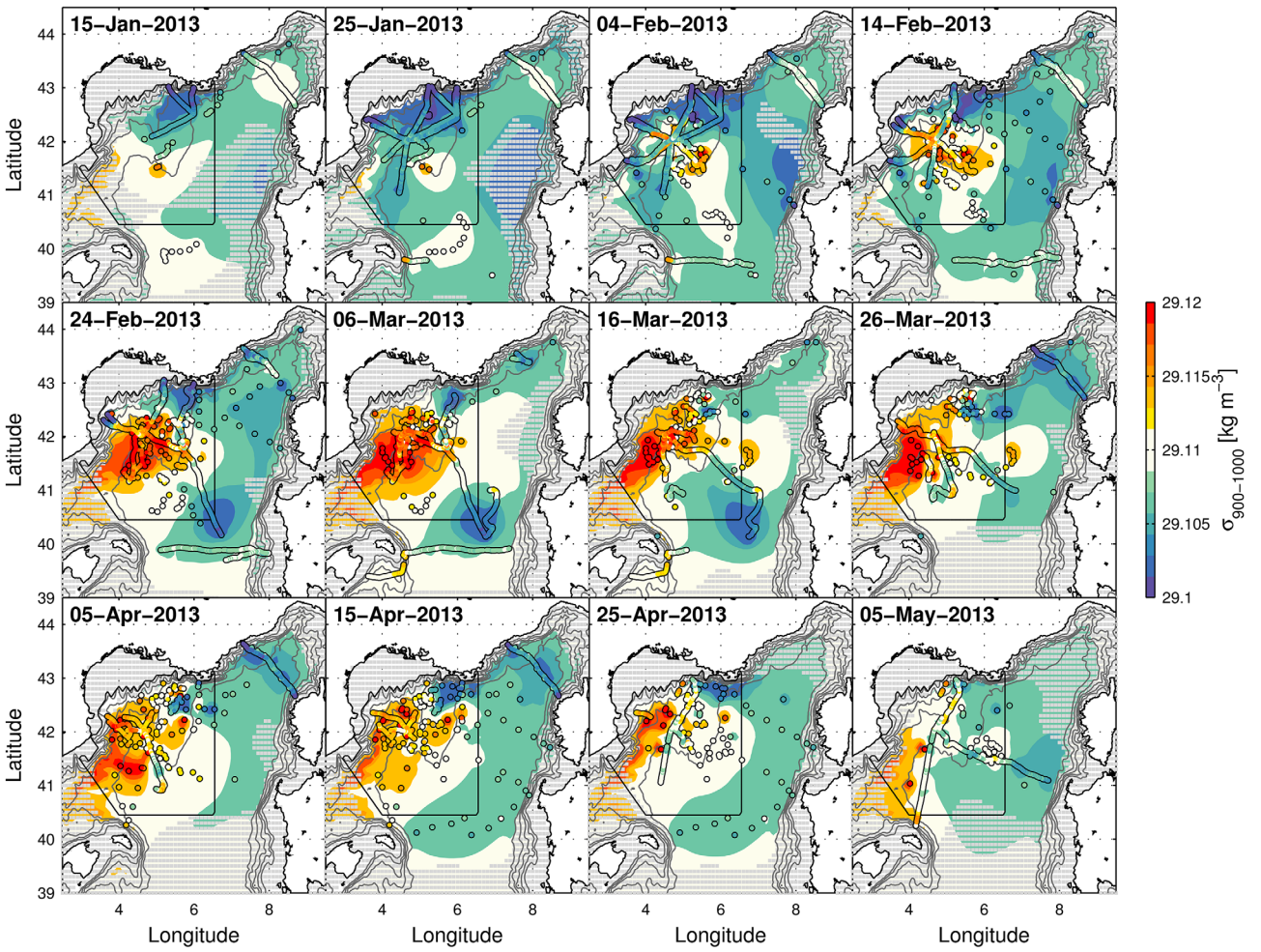

Figure 8. Objective analysis of potential density averaged over 900–1,000 m depth on a 10 day basis. The convection area used to assess deep water formation rates is delineated in black.

starting end of February for waters presenting densities < 29.11 kg m^{-3}. After a transformation in denser waters, the volume of this class of density increases from a minimum of -2.0 Sv (volume averaged over a year) compared to the situation on 5 January 2013 at a rate opposite and equivalent in magnitude to the general decrease of the volume of the denser water masses. At that time the volume of waters > 29.11 kg m^{-3} is consistently about $+2.0$ Sv (volume averaged over a year). This illustrates that the process of deep water formation by deep convection can be considered as a mass transfer that can be quantified, from the surface isopycnal layers loosing buoyancy due to air-sea interactions to the deep isopycnal layers.

The production of the densest waters (> 29.12 kg m^{-3}) is estimated at 0.5 Sv (Figure 9b, volume averaged over a year) and occurs when the mixing reaches the bottom. At that time, the atmospheric forcing remains intense for a while allowing to form even denser deep waters (Houpert et al., 2016). This layer presents a volume that increases until mid-March and decreases later on, as they spread and mix with lighter waters. The volume of the waters presenting potential densities > 29.115 and < 29.12 kg m^{-3} increases up to a maximum of 1.5 Sv (averaged over a year) in mid-March (Figure 9b). These deep waters form earlier with an increase in volume starting in early February and a first relative maximum in volume in mid-February at the time of the first event of deep convection. It then decreases until it increases again around mid-March at the time of the second deep convection event, in a consistent way with Figure 4. The evolution of the volume of the waters presenting potential densities > 29.11 and < 29.115 kg m^{-3} shows that they are the first to experience an increase of their volume during the winter. It starts to increase in mid-January and reaches

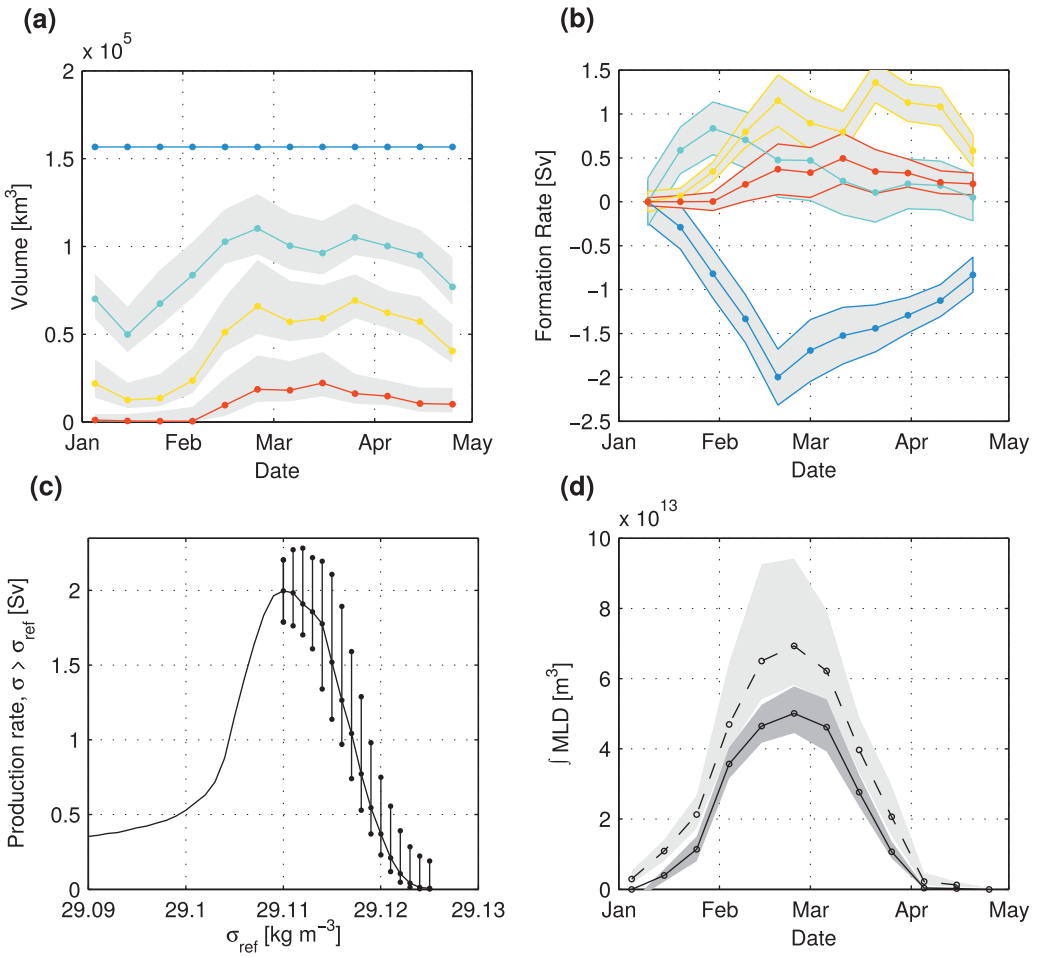

Figure 9. (a) Temporal evolution of the volume for waters presenting greater densities than 28.3 kg/m^3 (blue) corresponding to the minimum density observed in the deep convection area shown in Figure 8, 29.11 kg/m^3 (green), 29.115 kg/m^3 (yellow), and 29.12 kg/m^3 (red). Error bars in gray result from the optimal interpolation error. (b) Temporal evolution of the volume of water between consecutive isopycnals calculated by comparison to the situation on 5 January and reduced to Sv (volume averaged over 1 year) for waters presenting densities lower than 29.11 kg/m^3 (blue), between 29.11 kg/m^3 and 29.15 kg/m^3 (green), between 29.115 kg/m^3 and 29.12 kg/m^3 (yellow), and greater than 29.12 kg/m^3 (red). Error bars result from those of Figure 9a. (c) Volume of water denser than a given isopycnal produced between the 5 January and 24 February. Error bars are computed from the volume error of each density class of the optimal interpolation. For clarity, they are only plotted for waters undergoing a net volume increase during considered period. (d) Convective volume defined as the volume-integrated mixed layer. The continuous line represents this quantity for MLD greater than 1,000 m and the dashed line for MLD greater than 500 m. Error bars in gray result from the optimal interpolation error.

a maximum in mid-February. This increase is followed by a slow but continuous decrease until May at about the same rate as for the densest layers.

For 2013, we can conclude that deep-water formation has created water with potential densities $>$ 29.11 kg m^{-3} with a rate of formation which can be estimated to 2.0 $\pm$0.2 Sv (volume averaged over the year—see Figure 9c). In addition, this volume of deep water can be decomposed into two main categories: (1) deep water having a density $>$ 29.12 kg m^{-3} formed around the end of February starting once the mixing layer has reached the bottom (25% of volume formed); (2) deep water with a slightly lower density $>$ 29.11 kg m^{-3} formed starting at the beginning of February and composing most of the newly formed deep waters (75% of the volume). During the month of March, the second episode of mixing, appears to only generate a second-order formation rate of 0.1 Sv compared to the previous maximum observed in mid-February, the period of negative heat fluxes at that time being possibly too short to have a real significant impact on the water column.

These approaches by density classes may suggest there are different types of newly formed deep waters but in reality this is more a continuum of newly formed deep waters presenting densities between 29.11 and 29.123 (the maximum observed density) as illustrated by Figure 9c which inventories the volume (averaged over a year) of the different waters formed according to their density properties. Because it shows the dependency of the change of volume for waters having a greater density than, the production rate must be determined by the maximum of the curve and is consistently about 2.0 Sv (volume averaged over a year).

Finally, Figure 9d shows the volumes estimated using the MLD estimates which shows that there is instantaneously about 3 times less waters in relatively shallow mixed layer (deeper than 500 m) than in the very deep ones (deeper than 1,000 m) with volume estimates of maximum 7 10^{13} m^3 and 5 10^{13} m^3, respectively. The overall volume of newly formed deep waters that can be computed late February (when the volume is maximum) from this method is about 1.4 Sv (averaged over a year) using MLD $>$ 1,000 m and about 2.0 Sv (averaged over a year) using MLD $>$ 500 m.

7. Discussion

The analyses presented above do not account for small-scale processes, except in the "error" estimated on our 10 km $\times$ 10 km grid. This is so not critical as far as budgets are concerned but that somewhat hides a variety of processes at stake. After summarizing important results about related numerical studies and discussing the robustness of our deep water formation rate estimates, we will highlight in this section several peculiar circulation features that could be observed. Our observations bring new knowledge on the submesoscale turbulence, the *plumes* in the *Mixed Patch* and the symmetric instability at the edge of the *Mixed Patch* that are important to consider when studying deep convection and subsequent bloom because they are responsible for significant fluxes of energy and (dissolved and particulate, organic and inorganic) matter—in particular while analyzing/interpreting the various biogeochemical measurements carried out during the R/V cruises, and more especially during the DEWEX-1 and DEWEX-2 cruises which collected numerous biogeochemical observations based on water samples.

7.1. Numerical Model Initialization/Validation

The Summer data were used to correct initial conditions for modeling studies. As pointed out by Leger et al. (2016), "L'Hévéder et al. (2013) and Somot et al. (2016), numerical simulations are very sensitive to the initial conditions with regards to winter convection and numerical outputs, including operational products like MERCATOR PSY2V4R4 (Estournel et al., 2016b), have generally serious difficulties to describe well the intermediate and deep layers, because stratification is influenced by initial conditions derived from smoothed climatologies encompassing decades of observations. Waldman et al. (2017a) and Estournel et al. (2016b) showed it is possible to correct the initialization and forcing of their model and to significantly improve the realism of the simulations using the DEWEX data set both for initial conditions correction in Summer and later validation.

This data set was then used for validation purposes to assess the realism of numerical simulations in particular in terms of timing and geography of the phenomena as well as in terms of quantitative estimates of the deep water formation rate (Waldman et al., 2016, 2017b) and in terms of mesoscale and submesoscale processes (Damien et al., 2017; Waldman et al., 2017a) by performing similar diagnostics in the observations and the simulations, and sensitivity studies. They were thus able to reach a better understanding of deep convection processes from autumn to winter together with quantitative estimates. They were able in particular to estimate that lateral advection through the *Mixed Patch* could represent 58% of the destratifying effect of surface fluxes when integrated over the winter. This implies restratification must be considered as a major process during, and not only after the end of, the violent mixing but not as important as in the theory of Visbeck et al. (1996) in which lateral fluxes entirely balance the buoyancy loss through the sea surface, certainly because deep convection reached the bottom this year which cast a limit to the equilibrium depth solved in this study. The winter 2012–2013 is probably the third in buoyancy loss intensity after 2005 and 2012 during the period 1980–2013 (Somot et al., 2016) with more than 20 "stormy days" over the December–March period.

Another major outcome of this DEWEX experiment concerns the air-sea interactions. It must be noted it was impossible to measure directly the air-sea turbulent fluxes and that estimates of the total buoyancy

losses are dependent on their parameterization. It has not been particularly developed for strong winds as one can observe in this region in winter and this can introduce some uncertainty on the role of the atmosphere. Thanks to this data set, Caniaux et al. (2017) managed to propose an inverse method to estimate during 1 year heat and water fluxes for the whole northwestern Mediterranean basin and at a fine-scale resolution (i.e., hourly fluxes and 0.04° × 0.04° longitude, latitude) allowing to close the heat and freshwater budgets. The comparison of theses adjusted fluxes with fluxes estimated at the LION buoy from in situ meteo-oceanic measurements shows a good correlation ($r^2 = 0.96$) and provides a validation of the parameterization used for the estimates of the turbulent air-sea fluxes from the LION buoy (see Caniaux et al.'s Figure 9).

7.2. nWMDW Formation Rate Estimates

One shortcoming is that the frontier closing the domain used for estimating the deep water formation rate (see Figure 8) is relatively close to the *Mixed Patch* on its southwestern part. This could lead to underestimations of the volume formed. However, the dense water volume formed outside the domain is likely second order compared to our estimates. MLD barely $>$ 750 m (Figure 8) while potential densities $<$ 29.10 kg m^{-3} (Figure 8) are observed along this frontier and the chosen domain likely captures the entire deep convection process. In order to assess their robustness, our estimates of 2.0 Sv for the production of newly formed deep waters can be compared with estimates that can be made from different methodologies.

As already pointed out in section 6.3, the volume of water formed could be estimated assessing the maximum volume of the mixed layer greater than a given value, enough to have mixed the LIW layer lying above the deep waters but this induces some uncertainties related to the arbitrary choice of the threshold (see 9d: 1.4 Sv for MLD $>$ 1,000 m, 2.0Sv for MLD $>$ 500 m). Another but similar method is to use satellite ocean color images as in Houpert et al. (2016) and Herrmann et al. (2017), when the cloud coverage allows exploiting some images of the deep convection area. The strategy is to identify the "blue hole" associated to *Mixed Patch* within restratifying waters around. In 2013, using Figure 2e and estimating the "Blue Hole" surface with a threshold value of Chl-a $<$ 0.15 mg m^{-3} yields to 23 583 km^2. Considering an average depth of 2,200 m in the convection zone, the winter 2013 would thus present a production rate of 1.6 Sv (on average over the year). Again, it must be noted this method is very sensitive to the threshold (here in chl-a concentration): considering a slightly different threshold in Chl-a concentration of $<$ 0.25 mg m^{-3} would yield in fact to a doubling of the volume of the newly formed deep waters. There is so a strong need to accurately define the threshold in chl-a concentration used for such estimates. The choice of $<$ 0.15 mg m^{-3} can actually be justified by data from gliders crossing the edge of the *Mixed Patch* at about the date of the satellite image (Houpert et al., 2016). They show that deep mixed layers are associated with chl-a concentrations lower than this value this year but the right threshold is not necessarily the same every year and it is important to note there is a need to carry out such measurements in the long-term if one wants to address interannual variability using this method.

Our estimates from in situ data based on density classes are similar in magnitude to those estimates but still larger by about 0.0–0.6 Sv (on average over a year). On the other hand, such estimates are likely to underestimate the deep water formation rate first because they do not account for lateral fluxes. Moreover, the process of deep water renewal is a process that is not instantaneous and estimates made on the basis of an instantaneous image or snapshot inevitably underestimate the volume of newly formed deep waters. The dates of analyses of MLD (every 10 days) and the available satellite images (with small cloud cover) do not necessarily correspond to the date of the maximum extent of *Mixed Patch* (Blue Hole) and restratification processes are able to quickly recap mixed layers possibly hiding volumes of newly formed deep waters under the surface. Still, it is quite appealing that the estimates based on a single analysis or a single ocean color image are in such a good agreement with our present ones based on density classes.

Other estimates were performed by Waldman et al. (2016) using analyses of ship CTD data only and the deep water formation rate was estimated to be 2.3 ± 0.5 Sv. Ship data are the only data except for the mooring data that characterize the deep layers and the cruise plans were designed to estimate such volumes with large-scale surveys. Using an OSSE approach based on the simulation presented in Estournel et al. (2016b), Waldman et al. (2016) assessed the capacity of the CTD array to capture seasonal dense water variations, in terms of spatial distribution and the results indicate a low uncertainty related to space and time undersampling of the observing network because the cruises carried out at large scale provide

integrated information. Our present estimates of newly formed dense water volumes certainly rely on the same deep data and the estimates are consistently similar. The methodologies proposed for estimating the deep convection rate are complementary. In particular, Waldman et al. (2017a) have shown from a modeling study that the *Mixed Patch* volume computed as the volume of MLD > 1,000 m (or from a cold signature (<13°C) of intermediate waters (400–600m)) reached a lower value by 1.5×10^4 km^3 (0.4 Sv averaged over a year) than the dense water formation rate computed with the volume of waters denser than 29.11 kg m^{-3} in their run. Both estimates have different physical origins, the former resulting exclusively from the intense vertical mixing during the deep water formation events and the latter also resulting from lateral advection and mixing with surrounding waters.

Noteworthy, we present here a methodology that allows such estimates to be augmented with the data from the numerous autonomous platforms (gliders, profiling floats, moorings, drifter) that could continuously observe dense waters (Figure 9), sometimes only above 1,000 m (gliders and floats) or 2,000 m (floats) depths but this additional information is very significant, helping to describe the timing of the production at higher frequency as well as transfers between different classes of density. Compared to few satellite images in months, or 1–6 times a year thanks to MOOSE-GE-like cruises, the 10 days analyses based on in situ data represent a breakthrough for describing the deep convection phenomenon.

7.3. SCVs

As described more thoroughly in (Bosse, 2015), glider data revealed for the first time very warm (+0.4°C) and saline (+0.1) submesoscale and lenticular anticyclones at intermediate depth characterized by a small radius (5 km) and high Rossby (0.3) and Burger (0.7) numbers. Their cores are composed of marked LIW. Figure 10a shows two of them on the same glider section and this illustrates how numerous they can be. Roughly 10 are formed each year contributing significantly to the spreading of the LIW toward the subbasin interior. They have a lifetime order a year and can be quite numerous in the whole basin. They would be mainly formed by the combined action of turbulent mixing and flow detachment of the northward flow of LIW at the northwestern tip of Sardinia. Upwelling conditions along the western coast of Sardinia associated with a geostrophic southward surface flow could also play a key role in their formation process. These "Suddies" contain LIW from the formation region that is protected from mixing with the surroundings by dynamical barriers due to the high nonlinearity of the SCV flow (Bosse et al., 2017). They have thus a potential impact on winter mixing because they correspond to salt/heat inputs at intermediate depths and are associated with dynamical preconditioning of mixing (local doming of isopycnals). About 2–3 (or more?) of these eddies could be present in the deep convection area (as suggested by Figure 10a) and expose such LIW (and all associated dissolved or particle organic and inorganic matters) to winter mixing. The stratification index of such eddies shows they are preconditioning agents and deep convection will preferentially develop in these flows. In terms of ecosystem functioning, this could be a direct route from the SCV formation locations (mainly the northwestern tip of Sardinia) to the deep convection area and contact with the atmosphere.

In addition, Bosse et al. (2016) identified other SCVs, remnants of wintertime deep vertical mixing events. Figure 10b shows a transect across the boundary circulation (Northern Current and the south recirculation associated with the North Balearic Front) and the *Mixed Patch* with *Transition Zones* in-between, where SCVs can be observed, just expelled from the homogeneous *Mixed Patch*. Figure 10c also shows two of them (one cyclonic and one anticyclonic) on the same glider section, which again illustrates how numerous these eddies can be in Spring. This documents the spreading phase of deep convection with different eddies presenting different characteristics in temperature and salinity. These SCVs are though all characterized by a small radius (∼5–8 km), mostly strong depth-intensified orbital velocities (∼10–20 cm s^{-1}) with sometimes a surface signature, high Rossby (∼0.5) and Burger numbers O(0.5–1). Anticyclones are found to transport newly formed waters resulting from vertical mixing characterized by intermediate (∼300 m) to deep (∼2,000 m) mixing. Cyclones are characterized by a thick layer (∼500–2,000 m) of weakly stratified newly formed deep waters likely extending from the bottom of the ocean (∼2,500 m). Cyclones extending from the surface to the bottom have also been observed. All these SCVs result from intrusions of mixed fluid parcels into a more stratified environment and followed by cyclogeostrophic adjustment. Noteworthy, the formation of cyclonic eddies is favored in 2013 once the convection reached the bottom because this implies a limit in the adjustment phase and prevents the formation of anticyclones composed of nWMDW.

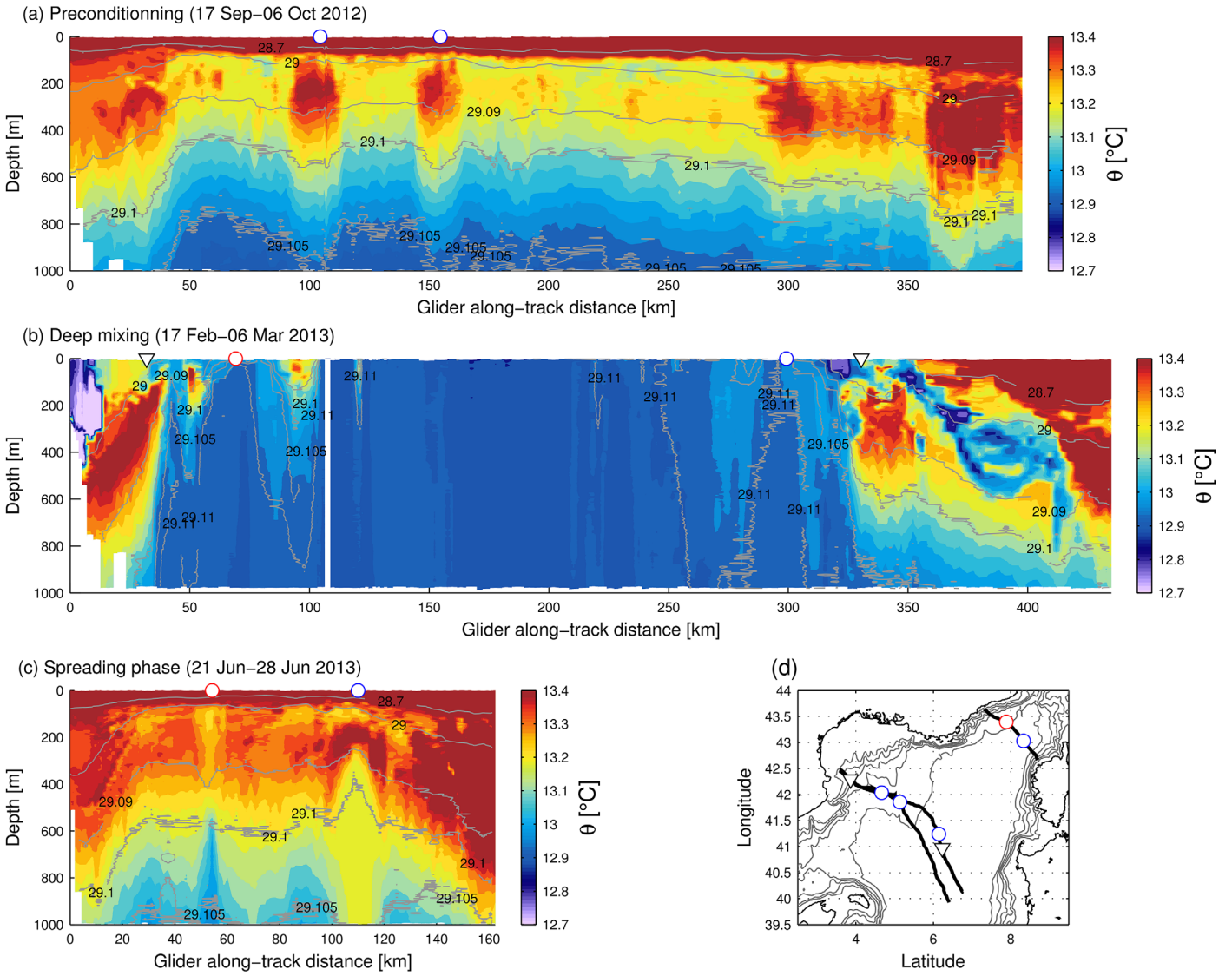

Figure 10. Glider potential temperature sections across the northwestern basin illustrating the role of SCVs during the (a) preconditioning, (b) violent mixing, and (c) spreading phases. White circles indicate locations of SCVs. White triangles indicate interleaving at the edge of the deep convection area.

Both anticyclonic and cyclonic SCVs have a prominent role in the spreading of the newly formed deep waters away from the winter mixing areas. Since they can survive until the following winter, they can greatly populate the basin and also have a great impact on the mixed layer deepening through a local preconditioning effect. These SCVs consist in another type of preconditioning agents like the above mentioned Suddies. Moreover, they can be formed throughout the deep convection mixing phase and modulate at this scale the vertical mixing occurring in *Plumes* during the violent mixing phase as well.

As reported by Bosse et al. (2017), they have a significant impact on the distributions of biogeochemical properties with clear signatures on the dissolved matter (nutrient and dissolved inorganic carbon in particular), compared to the surroundings. SCVs cores contain concentrations that are very contrasted with the general deep concentrations, being composed of waters resulting from a mixing of surface waters with deeper waters. This introduces a granularity at the SCV scale in the distributions of the biogeochemical variables in the basin since SCVs export these waters throughout the basin. Finally, these eddies have a peculiar impact on suspended particles distribution. As reported by Durrieu de Madron et al. (2017), there is evidence of bottom thick nepheloid layer formation coincident with deep sediment resuspension induced by bottom-reaching convection events. This bottom nepheloid layer, which presents a maximum thickness of

around 2,000 m in the center of the convection region, can persist within cyclonic nWMDW SCVs that are formed during the convection period and can last several months while traveling through the basin, still being associated with thick nepheloid layers far from the deep convection area. They are thus key mechanisms that control the concentration and characteristics of the suspended particulate matter in the basin, and in turn, affect the bathypelagic biological activity.

Waldman et al. (2017a, 2017b) have studied the impact of oceanic intrinsic variability on deep water formation with eddy resolving and permitting simulations. By comparing ensemble results they conclude mesoscale could have a significant impact on deep water formation. Resolving mesoscale significantly improves the realism in particular of the restratification/spreading phase and the *Mixed Patch* shape and extent. These are first estimates of the impact of such eddies even if the eddy-resolving simulation could not really account for SCVs. With a horizontal resolution of 1/36° (about 2 km), the simulation can actually not produce explicitly circulation features characterized by a radius order of 5 km but represent them thanks to subgrid parameterizations constrained by larger scale, but realist, variability and that allows a first assessment. The large increase of ocean intrinsic variability in eddy-resolving, compared to eddy-permitting, simulations, and of its impact on deep water suggests that SCVs could contribute largely to the chaotic ocean variability. Noteworthy, Damien et al. (2017) presented simulations which are the first ones to our knowledge that are able to simulate SCVs with similar dynamical characteristics and lifetimes in fully realistic conditions. A 1 km horizontal resolution and a great control of tracers and momentum horizontal diffusion seem to be decisive features to accurately resolve SCVs. This numerical study reveals itself particularly useful for refining the estimation of their integral effect and tracking them over their entire lifetimes. Further studies assessing the role played by SCVs in deep water formation (preconditioning, violent mixing, and spreading at basin-scale and interannual time-scale) and furthermore, in the different biogeochemical cycles that are identified in present biogeochemical numerical models forced by physical ones are now possible.

7.4. Plumes

Margirier et al. (2017) present a methodology based on a glider quasi-static flight model that was applied to infer the oceanic vertical velocity signal from the glider navigation data. Figure 11 shows an example showing the vertical trajectory of the glider being modified by vertical currents, the so-called *plumes*, and their estimates. Noteworthy, on the first apogee, one can see the glider was undergoing strong downward currents. It has nearly ended up with the loss of the glider (pressure rated to only 1,000 m) but the glider forward motion capacity allowed it to cross the vertical stream in about 10 min, and to reach a safer area,

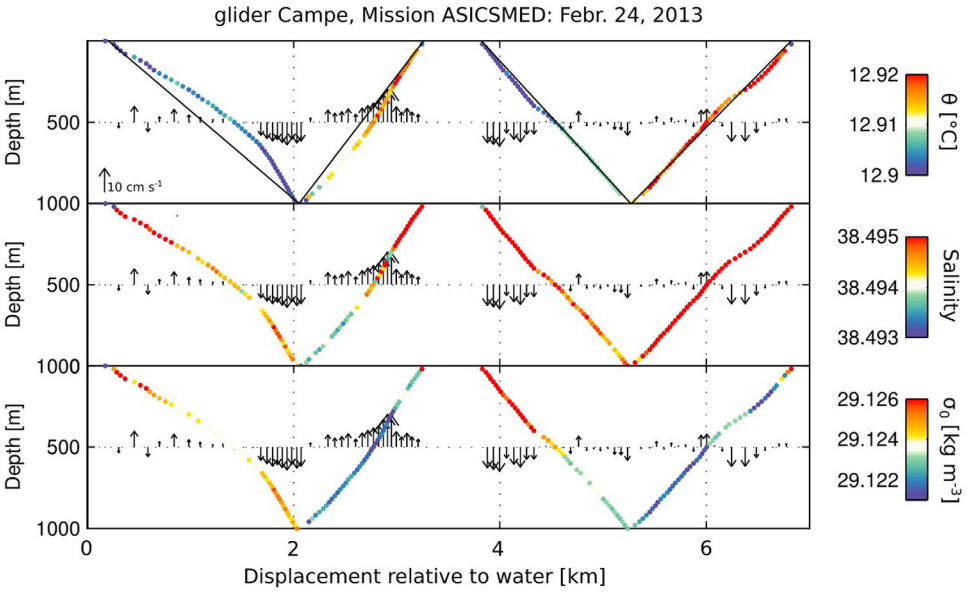

Figure 11. Vertical trajectory of a glider evolving in the *Mixed Patch* during violent mixing events color-coded with potential temperature, salinity, and potential density and estimates (black arrows) of oceanic vertical velocities based on the glider flight model presented in Margirier et al. (2017).

characterized by upward velocities. This illustrates the vertical currents are order of, and fortunately generally lower than, the vertical speed relative to water that glider can have, typically about $10-20$ cm.s^{-1}.

The data collected during winter 2012–2013 allows a first in situ statistical and 3-D characterization of the so-called *plumes* that are important mixing agents. During the active phase of mixing, significant oceanic vertical velocities (upward and downward, up to 18 cm.s^{-1} jostled the gliders. The gliders crossed many downward *plumes* with a mean radius of about 350 m and distant from each other by about 2 km on average. The upward part of the *plumes* is less coherent but apparently organized in crowns around the downward plumes. Much higher downward velocities were observed, with a magnitude about three times as large as that of the upward ones on average (–6.3 versus $+2.3$ cm.s^{-1}).

On average, the *plumes* cover 27% of the convection area and the upward motion associated with them covers 71%. The total of 98% provides confidence in coverage of the area. These are useful estimates to parameterize deep convection in ocean general circulation numerical models. A specific parameterization of convection has been introduced in atmospheric numerical models long ago but not yet in oceanic ones. Until now, oceanic numerical models that would need such a parameterization to represent mixing do use artificially increased diffusion instead. These results can now be used for the development and the testing (with all the data collected during our study period) of a convection parameterization in oceanic numerical models, following similar developments in meteorology for convection in the atmosphere that use the convective fraction of a grid cell as a key parameter, and further progress in modeling the deep convection processes can be soon expected.

The structure in temperature and salinity as well as biogeochemical properties (dissolved oxygen, fluorescence, turbidity) associated to this *plumes* is as follows: the downward waters are saltier ($+0.001$), colder (-0.005°C) and thus denser (0.0015 kg m^{-3}) than the surrounding upward ones. The downward waters are also slightly richer in oxygen and less fluorescent. This confirms the downward *plumes* participate to the ventilation of the waters and a dilution effect on Chl-a estimates (already mentioned previously when commenting Figure 4) while in the upward parts of the plumes, phytoplankton would benefit from nutrients being brought to the surface layers. On the other hand, there is no mean correlation on the turbidity signals despite individual signals in *plumes* but going both directions and this compensates on the average. The role of plumes as mixing agents on the suspended material distribution likely results from various factors. There could be some passive advection of turbidity signals from the surface (bloom) but also sometimes from the nepheloid layer when the mixing reaches it. In the deep convection region, intense horizontal currents favor resuspension over thick layers (100s m), with often a higher expression in turbidity in that layer than at the surface. In addition, suspended material have proper vertical downward speed and that increases the complexity of the suspended material fluxes in the presence of *plumes* tickling this nepheloid layer and lateral advection, through SCVs in particular.

7.5. Symmetric Instability

Figure 12 illustrates the symmetric instability phenomenon presenting interleaving patterns at the edge of the deep convection area over 0–500 m along the vertical and 20 km along the glider track. Figure 10 also shows similar patterns north and south of the deep convection area, with alternating cold and warm waters circulating, respectively, downward/outward and upward/inward of the deep convection area. Figure 12 provides a zoom and documents this circulation feature that has a signature on all measured variables with tongues of alternating high and low values in temperature and salinity but also in dissolved oxygen, chl-a concentration estimates, and turbidity. Noteworthy are the high chl-a estimates where the interleaving connects to the surface Figure 12d.

Almost all glider sections across the edge of the *Mixed Patch* exhibited similar interleaving patterns during the mixing period as shown in Figure 12. In the ocean, the lateral shears, fronts, and preexisting eddies make the horizontal gradients of density in mixed layers, thus the thermal wind build up. If the slope of the buoyancy surface is steeper than the absolute momentum surface, the slantwise convection will occur to release symmetric instability. That can propagate below the mixed layer and produce circulation features responsible for the observed interleaving patterns. As indicated by Marshall and Schott (1999), the slantwise convection induced by symmetric instability could maintain a vertical stratification in the region that is being actively mixed. Using in particular the data collected during our study period, Bosse (2015) showed that symmetric instability can develop particularly at the edge of the *Mixed Patch*, mainly where wind and

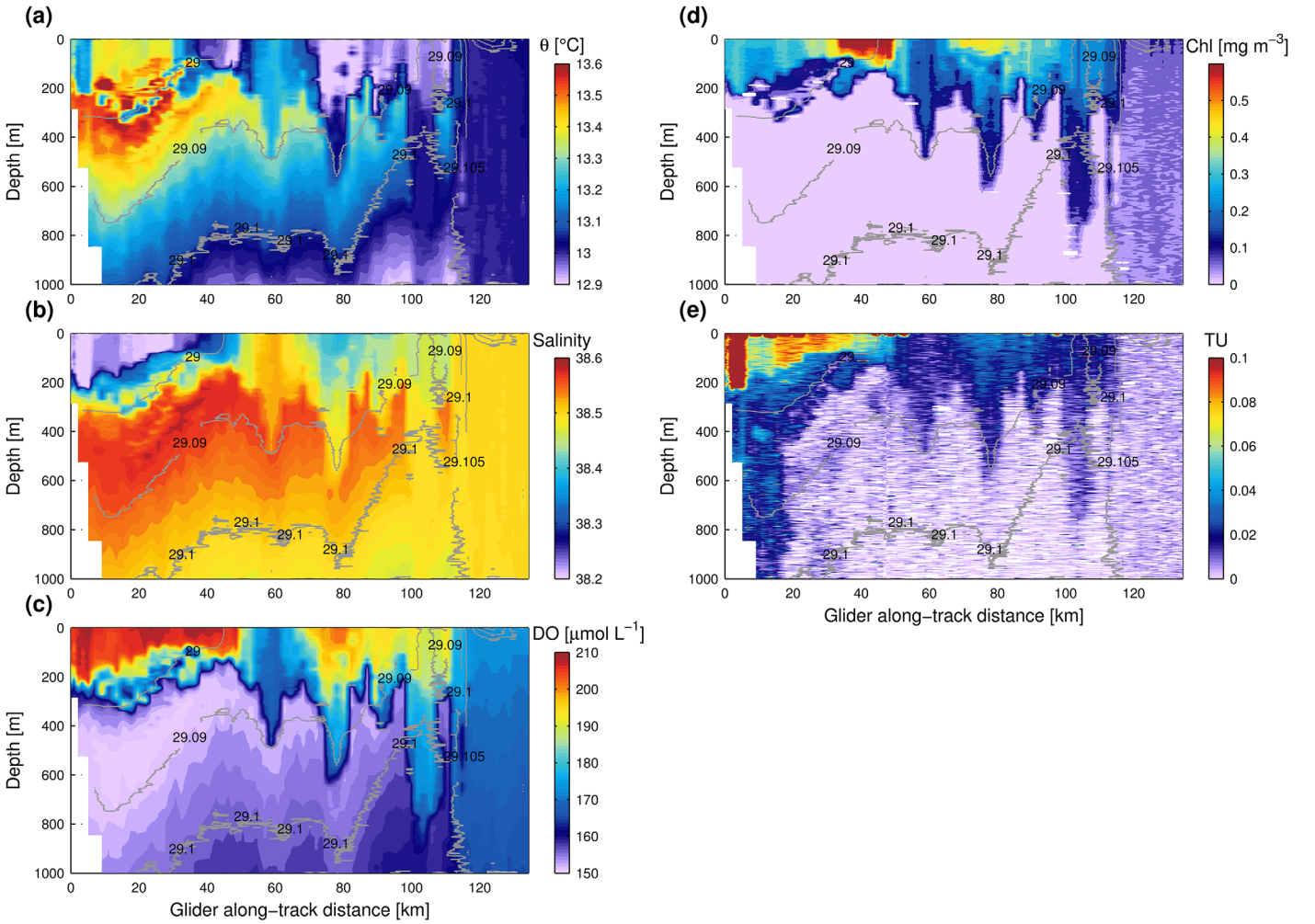

Figure 12. Glider sections across the *Transition Zone* between the Northern Current and the *Mixed Patch* of (a) potential temperature, (b) salinity, (c) dissolved oxygen (uncalibrated), (d) chl-a fluorescence, and (e) turbidity (uncalibrated).

currents flow along the same direction, and that it is possibly a major mixing process, like *plumes*, that needs to be taken into account to try to fully comprehend the deep convection phenomenon. The data collected by the gliders did allow to estimate the fluid Potential Vorticity (PV) and often showed patches of negative PV at the edge of the *Mixed Patch*, presenting a horizontal scale of a few kilometers and a vertical one of hundreds of meters. It is noteworthy the negative PV estimates are underestimated in absolute value. In fact, the gliders do not always sample the ocean exactly along the density gradients, which are thus underestimated, and if negative values could be observed, larger areas are certainly characterized by (and even more) negative PV values in reality. These negative patches indicate the edge of the *Mixed Patch* is a region where symmetric instability can develop even more broadly than in these local patches.

The glider data did allow estimates of the vertical velocities associated with plumes but not the part associated with symmetric instability. Estimating such vertical velocities is actually a major challenge for oceanography today. This type of signal is impossible to measure directly by in situ observations because of the weak signals of 1–10 mm s^{-1} that are supposed to be associated with such circulations. In addition, these vertical velocities are concentrated in small-scale and rapidly evolving flows that are nonlinear and ageostrophic (Mahadevan, 2006; Thomas et al., 2008). They are weak, but relatively steady and so important in terms of fluxes, compared to oscillating movements due to internal waves that likely mask them with vertical velocities of the order of 1 cm s^{-1} and this is even more the case with higher velocities observed in *plumes* during the violent mixing phase.

Analyzing numerical outputs in details can provide a clearer perception of this process. Using the NEMO model, Giordani et al. (2017) shows the edge of the *Mixed Patch* is a zone where negative PV can be observed and symmetric instability can develop as in the observations. In the high-resolution (1 km) SYMPHONIE model as well (see Damien et al. (2017) for a model description), there is a dominant and persistent negative PV frontal region of the Northern Current, where symmetrical instability can develop (Bosse, 2015) and Estournel et al. (2016b) showed that destratification of the surface layer in autumn occurs through an interaction of surface and Ekman buoyancy fluxes associated with displacements of the North Balearic front bounding the convection zone to the south. The Ekman buoyancy fluxes appear to be important also in autumn, deepening the mixed layer in the southwestern part of the cyclonic gyre, increasing the size of the preconditioned area, and possibly feeding such symmetric instability processes throughout the year when the wind is blowing down front.

The phenomenon can be described as follows. When the wind blows in the down front direction, the Ekman transport carries denser waters toward less dense waters. This induces not only a buoyancy flux but also the development of the symmetric instability phenomena with an associated steepening of isopycnals and increase of horizontal currents. This generates a potentially large turbulent mixing compared to the effect of surface buoyancy losses. This mechanical effect is important as indicated by Giordani et al. (2017) who estimated it is order of 4,000 W m^{-2}, about 4 times the maximum buoyancy losses at surface. The PV shows negative values when the front is particularly steep (steeper than momentum surfaces) and this indicates where/when the flow is unstable. The region of negative PV is characterized by a marked ageostrophy which tends to accentuate the destabilization of the fluid and to induce vertical motions trying to bring the fluid back to a geostrophic balance. At the interface between negative and positive PV, vertical velocities of about 100 m d^{-1} can develop tending to bring fluid particles of positive vorticity towards the surface and negative vorticity to greater depth. Thereafter, the front would evolve rapidly toward a more stable situation with less inclined isopycnals and a wider frontal area. In both observations and numerical simulation, the effect of this instability can be observed over great depths, much deeper than the mixed layer above.

The negative PV regions tend to fade away after about 24 h in the model simulations. Consequently, the frequent physical and biogeochemical observations carried out by gliders that suggest strong vertical motions, because of the observed interleaving of the different physical and biogeochemical observed variables and negative PV estimates, may be only observations of remnants of vertical motions due to symmetric instability. Though they provide clear evidence of the prominence of this phenomenon, higher repeat rates for glider observations would be required to actually resolve it. Crossing the northern Current and the frontal area (about 30–50 km width) takes about 1 or 2 days for a single glider and more gliders along the same repeat-sections would be required to increase the repeat rate if one wants to really capture this phenomenon.

Overall, symmetric instability appears to be a major process in deep convection inducing water masses mixing during the three deep convection phases as suggested by the high number of occurrences of glider observations of this phenomenon throughout the year and the numerical simulations. Vertical motions can be indeed induced during any down front wind event. This could be active at high temporal frequency and participate to a significant part of the water formed by intermediate and deep convection during winter and more indirectly throughout the year by participating to the preconditioning of the area. This could also explain why the mixing seems to occur preferentially during the first stages in the western part of the Gulf of Lions (see Figure 7), where northerly winds blow down front, above a southward ocean general circulation.

8. Conclusions and Outlook

In this review, we have attempted to draw together results of observations and numerical experiments in the context of 2012–2013 DEWEX field campaigns, to summarize our current understanding of the underlying hydrodynamic processes at work before, during, and after deep ocean convection events in the northwestern Mediterranean Sea and the interplay between the large scales, mesoscales, submesoscales, and convective scales. This interplay is complex since it involves scales, ranging from the scale of the general circulation, right down to the plumes at scales of <1 km, through eddies about the deformation radius (O(5 km) during winter period in the mixing area). As Marshall and Schott (1999) pointed out, a major

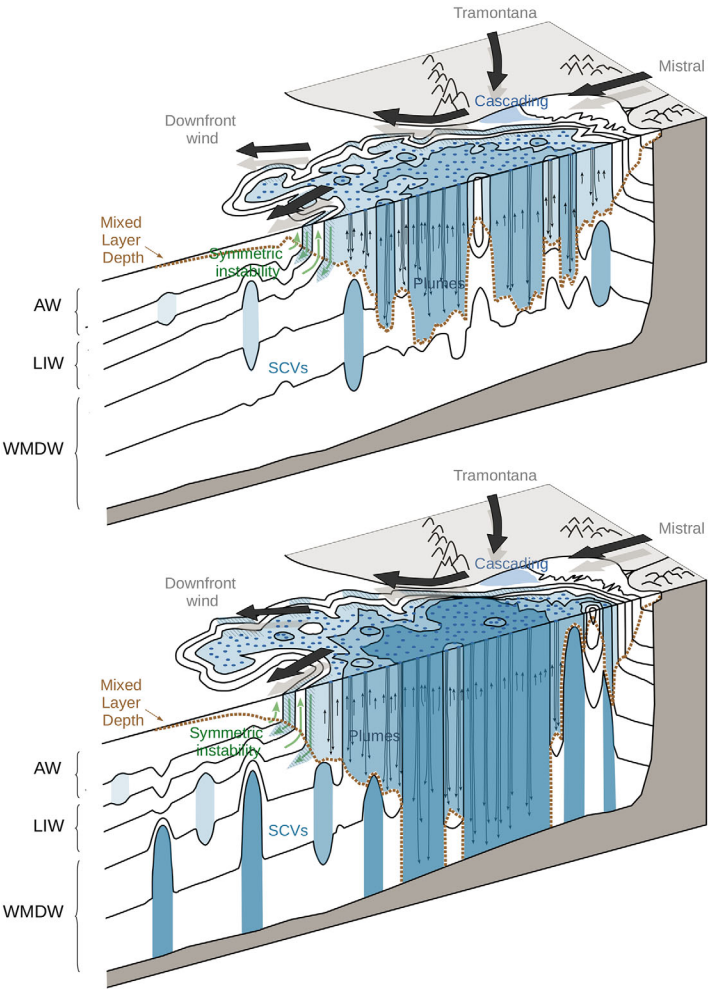

Figure 13. Schematic diagram of the evolution of the convection area during the violent mixing phase in a period of 1–2 weeks. Underlying stratification/outcrop is shown by selected isopycnals (continuous black lines). The volume of fluid just mixed by convection is shaded and color coded according to potential density classes.

challenge is to transform the obtained insights into parametric representations that address the complex 3-D nature of the processes at work. We have made a major step forward in that direction, about 15 years later, with a better description of the processes thanks to the autonomous platform technology, and can now consider not only some qualitative but also some quantitative aspects concerning deep convection. Deep convection is very difficult to observe due to its multiscale variability and because it happens during severe weather events that generally prevents the use of ships. We have demonstrated that the massive—and artful—deployment of autonomous platforms in combination with more classical research cruises, can change the way we perceive the oceanic environment, allowing us to reach a much better spatiotemporal coverage. There is a paradigm change with the use of mobile platforms, such as gliders and profiling floats. Although, this concerns a limited number of physical and biogeochemical variables (the ones measured by miniaturized sensors that can equip such platforms: temperature, salinity, currents, oxygen concentration, chl-a concentration, turbidity estimates, etc.), this allows to better comprehend the deep convection and subsequent bloom phenomena at various scales.

Deep convection and subsequent bloom have revealed ever greater complexity. Noteworthy are key elements that appear to be prominent for deep convection and subsequent bloom. The summer stratification is certainly key as it will be eroded continuously until the vertical mixing reaches great depths. Horizontal inhomogeneities in density in the mixed layer modulate its deepening, while fronts sharpen and (baroclinic) instability processes develop and produce a mesoscale turbulence. When the vertical mixing has eroded the LIW layer, it can reach quickly great depths (in about 1–2 weeks) and produce nWMDW resulting from mixing of the underlying WMDW with the water resulting from the mixing of AW and LIW above. Plumes develop with a downward plume radius of about 350 m over a turbulent flow presenting a scale of about 5 km embedded in the general circulation and ultimately forming the long-lived SCVs. The location of such intense vertical mixing is mainly due to preconditioning effects at various scales (gyre, mesoscale, submesoscale) as sketched in Figure 13, that is interesting to consider together with Figures 6–8 for the large-scale aspects and Figures 10 and 12 for the smaller ones. Submesoscale turbulence and horizontal transfers shape a deep mixing area in the center of the basin gyre circulation that is surrounded by a *Transition Zone* where lateral exchanges are prominently located between the Mixed Patch and the boundary circulation (Northern Current and its recirculation along the North Balearic Front). In about 1–2 weeks, several storms induce several mixing events and restratification ones in-between that ultimately produce a water column that is mixed from the surface to the bottom. The SCV phenomenology appears to be key for understanding the deep convection process because of their role in preconditioning and lateral exchanges. In addition, symmetric instability develops along fronts under down front winds, which vertically and horizontally mixes the waters from each side of the fronts and make typical interleaving patterns emerge. The preconditioning and the spreading occur during the violent mixing phase. When the buoyancy loss stops, much of the flow and the spreading of water masses is eddy-dominated and highly variable while serious recapping processes concur due to both heat (and freshwater) gain and oceanic instabilities. Herein lies the reason why deep convection is such an interesting phenomenon from a theoretical point of view and why it is such a challenging and demanding process to observe and model.

Our multiplatform approach allowed to have more synoptic observations and provided new results on deep convection. This can be considered as a major step forward compared to previous studies limited to

very few in situ observations of the water column. Our observations allow performing first budgets and assessments with a continuity and accuracy that was never reached before in terms of potential temperature, salinity, MLD, APE, KE, EKE, formation rates but also estimates of chl-a based on in situ data. They also provide a new and nice description of several types of the SCVs, especially along the vertical, including new (or first time identified as such) circulation features like the long-lived cyclonic SCVs. They also allowed a first statistical description of plumes and provided a first in situ indication of the importance of symmetric instability, all around the deep convection area, down front winds in meanders in the South and in a more pronounced way along the Northern Current where the topographic constraint orients more generally the flow along Mistral and Tramontane winds. Not only the processes are becoming clearer from a physical point of view but also their prominent impact and significance for biological processes.

The budgets and diagnostics presented in this paper can be made in numerical models as well and we advocate that models should be able to produce the same results as presented here, to be considered as presenting a high realism in simulating the deep convection process (and subsequent bloom) and as able to provide relevant conclusions on particular processes and climate projections. The observations carried out in 2012–2013 could be considered as a first benchmark and a lot of further progress in the (physical and biogeochemical) modeling of deep convection, and subsequent bloom phenomena can be expected by further comparing these observations and numerical simulations.

Moreover, the data set collected from ships and autonomous platforms (gliders, profiling floats, moorings, surface drifters) offers an invaluable context for observations based on water samples from ship data. While ship surveys allowed delayed-mode quality control for data collected by autonomous platforms, they were augmented by a better spatiotemporal coverage for a few physical/bio-optical variables. Noteworthy, this could be extended to estimate budgets for other variables with conditional objective analyses methods and work is in progress to estimates budgets for biogeochemical variables that are more scarcely observed. Furthermore, with the addition of numerical modeling and data assimilation, a further insight of the deep convection and subsequent bloom phenomena can be reasonably expected. The DEWEX framework has already motivated many studies based on both observations and modeling and this will be furthermore developed, in particular with respect to biogeochemical theory and modeling. Many studies have already used this wonderous data set and many others can be legitimately anticipated. There is still a lot to investigate and we dare anticipate this will go beyond this special issue.

It was urgent and timely to carry out this experiment, in such a way a first spatiotemporal coverage (from an in situ point of view) providing adequate initialization information is available for 2012–2013, while embedded in the less intense but on the long-term observational framework of MOOSE. While the fluxes (from atmospheric models) are more and more validated, the monitoring of some of the resultant changes in the system is now feasible with modern techniques, and this must be done from now in a more global and fit-for-purpose Mediterranean GOOS (Global Ocean Observing System) program encompassing the whole Mediterranean Sea that can address critical societal issues at this scale. In the future, the knowledge will narrow and more frequent (spatiotemporal) data set will be possible and required to further investigate and monitor the processes. There must be concerted efforts in developing both the spatiotemporal coverage of the in situ observing systems (in combination with satellites) and the number of variables that can be observed in an autonomous way. The long-term observations will serve as a backbone for further understanding at the process level on an interannual basis while one can anticipate further and more intense process studies will be developed. As the miniaturization of sensors will increase, the number, the diversity of platforms, and sensors on-board will likely unlock our knowledge on many processes/cycles, and transports of energy and various matter in the ocean.

We presented an approach that was not only quite successful but especially scalable, and this motivates to develop the same multiplatform/multiscale strategy for other areas/processes. What has been learned about how to operate such a complex program is that preparation, coordination, and funding are key aspects and it was only possible to achieve it building on several national and European infrastructures and several research programs. No call for proposals could be solely solicited to achieve such an experiment and we hope this will change in the future for the sake of simplicity and continuous knowledge improvements.

Acknowledgments
Hydrographical data were collected and made freely available by the Coriolis project (http://www.coriolis.eu.org) and programs that contribute. We would like to acknowledge the staff of the French National Pool of Gliders (DT-INSU/CNRS-CETSM/Ifremer) for the sustained gliders deployments carried out in the framework of MOOSE, as well as the intensive deployments during this 2012–2013 DEWEX experiment and to warmly thank Captains and crews of R/V *Le Tethys II* (CNRS/INSU, France), R/V *Le Provence* (Phares et Balises, France), and R/V *Le Suroît* (Ifremer, France) and R/V *Urania* (CNR, Italy), as well as all scientists, engineers, technicians, and students who participated to the MOOSE-GE, HyMeX/SOP1 and SOP2, DEWEX, and DOWEX different cruises and autonomous platforms deployments. Support was provided by the French "Chantier Méditrranée" MISTRALS program (HyMeX and MERMeX components), the ANR ASICSMED project (ANR 12-BS06-0003), the MOOSE long-term observatory (SOERE/AllEnvi-SNO/INSU), the Bio-Argo project (CNES-TOSCA), and the ANR NAOS project (ANR J11R107F), as well as the NATO STO-CMRE NOMR12 experiment. Support was also provided by the EU projects FP7 GROOM (grant agreement 284321), FP7 PERSEUS (grant agreement 287600), FP7 JERICO (grant agreement 262584), and the COST Action ES0904 "EGO" (Everyone's Gliding Observatories).

References

Adloff, F. Somot, S., Sevault, F., Jordà, G., Aznar, R., Déqué, M., . . . Gomis, D. (2015). Mediterranean Sea response to climate change in an ensemble of twenty first century scenarios. *Climate Dynamics*, *45*, 2775–2802. https://doi.org/10.1007/s00382-015-2507-3

Auger, P., Ulses, C., Estournel, C., Stemman, L., Somot, S., & Diaz, F. (2014). Interannual control of plankton ecosystem in a deep convection area as inferred from a 30-year 3d modeling study: Winter mixing and prey/predator in the NW Mediterranean. *Progress in Oceanography*, *124*, 12–27.

Béthoux, J.-P., Durieu de Madron, X., Nyffeler, F., & Tailliez, D. (2002). Deep water in the western Mediterranean: Peculiar 1999 and 2000 characteristics, shelf formation hypothesis, variability since 1970 and geochemical inferences. *Journal of Marine Systems*, *33–34*, 117–131. https://doi.org/10.1016/S0924-7963(02)00055-6

Boehme, L., & Send, U. (2005). Objective analyses of hydrographic data for referencing profiling float salinities in highly variable environments. *Deep Sea Research Part II: Topical Studies in Oceanography*, *52*(3–4), 651–664. https://doi.org/10.1016/j.dsr2.2004.12.014

Bosse, A. (2015). *Circulation générale et couplage physique-biogéochimie à (sous-)mésoéchelle en Méditerranée Nord-occidentale à partir de données in situ* (PhD thesis). Paris, France: Université Pierre et Marie Curie.

Bosse, A., Testor, P., Houpert, L., Damien, P., Prieur, L., Hayes, D., . . . Mortier, L. (2016). Scales and dynamics of submesoscale coherent vortices formed by deep convection in the northwestern Mediterranean sea. *Journal of Geophysical Research: Oceans*, *121*, 7716–7742. https://doi.org/10.1002/2016JC012144

Bosse, A., Testor, P., Mayot, N., Prieur, L., D'Ortenzio, F., Mortier, L., . . .Raimbault, P. (2017). A submesoscale coherent vortex in the Ligurian sea: From dynamical barriers to biological implications. *Journal of Geophysical Research: Oceans*, *122*, 6196–6217. https://doi.org/10.1002/2016JC012634

Bosse, A., Testor, P., Mortier, L., Prieur, L., Taillandier, V., D'ortenzio, F., & Coppola, L. (2015). Spreading of Levantine Intermediate Waters by submesoscale coherent vortices in the northwestern Mediterranean Sea as observed with gliders. *Journal of Geophysical Research: Oceans*, *120*, 1599–1622. https://doi.org/10.1002/2014JC010263

Bouin, M.-N., & Rolland, J. (2011). *Lion mto-france buoy 0–250 m ocean temperature mooring line, pyranometer and pyrgeometer, sea surface temperature and salinity* (technical report). Retrieved from https://doi.org/10.6096/MISTRALS-HyMeX-MOOSE.388; https://doi.org/10.6096/HyMeX.LionBuoy.Pyranometer.20100308; https://doi.org/10.6096/MISTRALS-HyMeX-MOOSE.1025

Cacho, I., Grimalt, J., & Canals, M. (2002). Response of the western Mediterranean sea to rapid climatic variability during the last 50,000 years: A molecular biomarker approach. *Journal of Marine Systems*, *33*, 253–272.

Caniaux, G., Prieur, L., Giordani, H., & Redelsperger, J.-L. (2017). An inverse method to derive surface fluxes from the closure of oceanic heat and water budgets: Application to the north-western Mediterranean sea. *Journal of Geophysical Research: Oceans*, *122*, 2884–2908. https://doi.org/10.1002/2016JC012167

Coll, M., Piroddi, C., Steenbeek, J., Kaschner, K., Ben Rais Lasram, F., Aguzzi, J., . . .Voultsiadou, E. (2010). The biodiversity of the Mediterranean sea: Estimates, patterns, and threats. *PLoS One*, *5*(8), e11842. https://doi.org/10.1371/journal.pone.0011842

Conan, P. (2013). *DEWEX-MERMEX 2013 LEG2 cruise, RV Le Suroît* (technical report). Retrieved from https://doi.org/10.17600/13020030

Conan, P., Søndergaard, M., Kragh, T., Thingstad, F., Pujo-Pay, M., Williams, P. J. le B., . . . Riemann, B. (2007). Partitioning of organic production in marine plankton communities: The effects of inorganic nutrient ratios and community composition on new dissolved organic matter. *Limnology and Oceanography*, *52*(2), 753–765.

Coppola, L., Prieur, L., Taupier-Letage, I., Estournel, C., Testor, P., Lefevre, D., . . . Taillandier, V. (2017). Observation of oxygen ventilation into deep waters through targeted deployment of multiple argo-o2 floats in the north-western Mediterranean Sea in 2013. *Journal of Geophysical Research: Oceans*, *122*, 6325–6341. https://doi.org/10.1002/2016JC012594

Damien, P., Bosse, A., Testor, P., Marsaleix, P., & Estournel, C. (2017). Modeling postconvective submesoscale coherent vortices in the northwestern Mediterranean sea. *Journal of Geophysical Research: Oceans*, *122*, 9937–9961. https://doi.org/10.1002/2016JC012114

D'Ortenzio, F., Lavigne, H., Besson, F., Claiustre, H., Coppola, L., Garcia, N., . . . Testor, P. (2014). Observing mixed layer depth, nitrate and chlorophyll concentrations in the northwestern Mediterranean: A combined satellite and NO3 profiling floats experiment. *Geophysical Research Letters*, *41*, 6443–6451. https://doi.org/10.1002/2014GL061020

Ducrocq, V., Braud, I., Davolio, S., Ferretti, R., Flamant, C., Jansa, A., . . . Tamayo, J. (2014). Hymex-sop1, the field campaign dedicated to heavy precipitation and flash-flooding in the northwestern Mediterranean. *Bulletin of the American Meteorological Society*, *95*, 1083–1100, https://doi.org/10.1175/BAMS-D-12-00244.1

Durrieu de Madron, X., Guieu, C., Sempéré, R., Conan, P., Cossa, D., D'Ortenzio, F., . . . Verney, R. (2011). Marine ecosystems' responses to climatic and anthropogenic forcings in the Mediterranean. *Progress in Oceanography*, *91*(2), 97–166. https://doi.org/10.1016/j.pocean.2011.02.003

Durrieu de Madron, X., Houpert, L., Puig, P., Sanchez-Vidal, A., Testor, P., Bosse, A., . . . Raimbault, P. (2013). Interaction of dense shelf water cascading and open-sea convection in the northwestern Mediterranean during winter 2012. *Geophysical Research Letters*, *40*, 1379–1385. https://doi.org/10.1002/grl.50331

Durrieu de Madron, X., Ramondenc, S., Berline, L., Houpert, L., Bosse, A., Martini, S., . . . the ANTARES collaboration (2017). Deep sediment resuspension and generation and thick nepheloid layer generation by open-ocean convection. *Journal of Geophysical Research: Oceans*, *122*, 2291–2318. https://doi.org/10.1002/2016JC012062

Estournel, C., Testor, P., Damien, P., D'Ortenzio, F., Marsaleix, P., Conan, P., . . .Prieur, L. (2016b). High resolution modeling of dense water formation in the north-western Mediterranean during winter 2012–2013: Processes and budget. *Journal of Geophysical Research: Oceans*, *121*, 5367–5392. https://doi.org/10.1002/2016JC011935

Estournel, C., Testor, P., Taupier-Letage, I., Bouin, M.-N., Coppola, L., Durand, P., . . .Somot, S. (2016a). Hymex-sop2: The field campaign dedicated to dense water formation in the northwestern Mediterranean, *Oceanography*, *29*(4), 196–206. https://doi.org/10.5670/oceanog.2016.94

Fairall, C., Bradley, E., Hare, J., Grachev, A., & Edson, J. (2003). Bulk parameterization of air-sea fluxes: Updates and verification for the co-are algorithm. *Journal of Climate*, *16*, 571–591.

Garau, B., Ruiz, S., Zhang, W. G., Pascual, A., Heslop, E. E., Kerfoot, J., & Tintoré, J. (2011). Thermal lag correction on Slocum CTD glider data. *Journal of Atmospheric and Oceanic Technology*, *28*(9), 1065–1071. https://doi.org/10.1175/JTECH-D-10-05030.1

Gascard, J.-C. (1978). Mediterranean deep water formation baroclinic instability and oceanic eddies. *Oceanologica Acta*, *1*(3), 315–330.

Gascard, J-C., Watson, A. J., Messias, M.-J., Olsson, K. A., Johannessen, T., & Simonsen, K. (2002). Long-lived vortices as a mode of deep ventilation in the Greenland Sea. *Nature*, *416*, 525–527.

Gieskes, W. W., & Kraay G. W. (1983). Unknown chlorophyll a derivatives in the north sea and the tropical Atlantic ocean revealed by HPLC analysis. *Limnology and Oceanography*, *28*, 757–766.

Giordani, H., Lebeaupin-Brossier, C., Leger, F., & Caniaux, G. (2017). A PV-approach for dense water formation along fronts: Application to the northwestern Mediterranean. *Journal of Geophysical Research: Oceans*, *122*, 995–1015. https://doi.org/10.1002/2016JC012019

Giorgi, F. (2006). Climate change hotspots. *Geophysical Research Letters*, *33*, L08707. https://doi.org/10.1029/2006GL025734

Herrmann, M., Auger, P.-A., Ulses, C., & Estournel, C. (2017). Long-term monitoring of ocean deep convection using multisensors altimetry and ocean color satellite data. *Journal of Geophysical Research: Oceans*, *122*, 1457–1475. https://doi.org/10.1002/2016JC011833

Herrmann, M., Estournel, C., Adloff, F., & Diaz, F. (2014). Impact of climate change on the northwestern {Mediterranean}{Sea} pelagic planktonic ecosystem and associated carbon cycle. *Journal of Geophysical Research: Oceans*, *119*, 5815–5836. https://doi.org/10.1002/2014JC010016

Herrmann, M. J., Diaz, F., Estournel, C., Marsaleix, P., & Ulses, C. (2013). Impact of atmospheric and oceanic interannual variability on the Northwestern Mediterranean Sea pelagic planktonic ecosystem and associated carbon cycle. *Journal of Geophysical Research: Oceans*, *118*, 5792–5813. https://doi.org/10.1002/jgrc.20405

Herrmann, M. J., & Somot, S. (2008). Relevance of ERA40 dynamical downscaling for modeling deep convection in the Mediterranean Sea. *Geophysical Research Letters*, *35*, L04607. https://doi.org/10.1029/2007GL032442

Houpert, L. (2013). *Contribution to the study of transfer processes from the surface to the deep ocean in the Mediterranean Sea using in situ measurements* (PhD thesis). Perpignan, France: Université de Perpignan.

Houpert, L., Durrieu de Madron, X., Testor, P., Bosse, A., D'Ortenzio, F., Bouin, M. N., . . . Raimbault, P. (2016). Observations of open-ocean deep convection in the northwestern Mediterranean sea: Seasonal and interannual variability of mixing and deep water masses for the 20072013 period. *Journal of Geophysical Research: Oceans*, *121*, 8139–8171. https://doi.org/10.1002/2016JC011857

Jones, H., & Marshall, J. (1997). Restratification after deep convection. *Journal of Physical Oceanography*, *27*, 2276–2287. https://doi.org/10.1175/1520-0485(1997)027 <2276:RADC >2.0.CO;2

Killworth, P. (1976). The mixing and spreading phase of Medoc 1969. *Progress in Oceanography*, *7*, 59–90.

Killworth, P. (1979). On "chimney" formation in the ocean. *Journal of Physical Oceanography*, *9*, 531–554.

Lavigne, H., D'ortenzio, F., Claustre, H., & Poteau, A. (2012). Towards a merged satellite and in situ fluorescence ocean chlorophyll product. *Biogeosciences*, *9*(6), 2111–2125. https://doi.org/10.5194/bg-9-2111-2012

Lavigne, H., D'ortenzio, F., Migon, C., Claustre, H., Testor, P., Ribera D'alcalà, M., . . . Prieur, L. (2013). Enhancing the comprehension of mixed layer depth control on the Mediterranean phytoplankton phenology. *Journal of Geophysical Research: Oceans*, *118*, 3416–3430. https://doi.org/10.1002/jgrc.20251

Lebeaupin-Brossier, C., Arsouze, T., Beranger, K., Bouin, M.-N., Bresson, E., Ducrocq, V., . . . Taupier-Letage, I. (2014). Ocean mixed layer responses to intense meteorological events during hymex-sop1 from a high-resolution ocean simulation, *Ocean Modelling*, *84*, 84–103. https://doi.org/10.1016/j.ocemod.2014.09.009

Leger, F., Brossier, L. C., Giordani, H., Arsouze, T., Beuvier, J., Bouin, M.-N., . . .Nuret, M. (2016). Dense water formation in the north-western Mediterranean area during hymex-sop2 in 1/36 ocean simulations: Sensitivity to initial conditions. *Journal of Geophysical Research: Oceans*, *121*, 5549–5569. https://doi.org/10.1002/2015JC011542

Legg, S., & Marshall, J. C. (1993). A Heton model of the spreading phase of open-ocean deep convection. *Journal of Physical Oceanography*, *23*, 1040–1056. https://doi.org/10.1175/1520-0485(1993)023<1040:AHMOTS>2.0.CO;2

Legg, S., & McWilliams, J. C. (2001). Convective modifications of a geostrophic eddy field. *Journal of Physical Oceanography*, *31*, 874–891. https://doi.org/10.1175/1520-0485(2001)031<0874:CMOAGE>2.0.CO;2

Legg, S., McWilliams, J., & Gao, J. (1998). Localization of deep ocean convection by a mesoscale eddy. *Journal of Physical Oceanography*, *28*, 944–970. https://doi.org/10.1175/1520-0485(1998)028 <0944:LODOCB >2.0.CO;2

Le Traon, P. Y. (1990). A method for optimal analysis of fields with spatially variable mean. *Journal of Geophysical Research*, *95*(C8), 13543–13547. https://doi.org/10.1029/JC095iC08p13543

L'hévéder, B., Li, L., Sevault, F., & Somot, S. (2013). Interannual variability of deep convection in the northwestern Mediterranean simulated with a coupled AORCM. *Climate Dynamics*, *41*(3), 937–960. https://doi.org/10.1007/s00382-012-1527-5

Lilly, J. M., Rhines, P. B., Visbeck, M., Davis, R. E., Lazier, J. R. N., Schott, F., & Farmer, D. (1999). Observing deep convection in the Labrador Sea during Winter 1994/95. *Journal of Physical Oceanography*, *29*, 2065–2098. https://doi.org/10.1175/1520-0485(1999)029<2065:ODCITL>2.0.CO;2

Madec, G., Chartier, M., Delecluse, P., & Crépon, M. (1991). A three-dimensional numerical study of deep-water formation in the northwestern Mediterranean Sea. *Journal of Physical Oceanography*, *21*, 1349–1371.

Mahadevan, A. (2006). Modeling vertical motion at ocean fronts: Are nonhydrostatic effects relevant at submesoscales? *Ocean Modelling*, *14*(3–4), 222–240. https://doi.org/10.1016/j.ocemod.2006.05.005

Margirier, F., Bosse, A., Testor, P., L'hvder, B., Mortier, L., & Smeed, D. (2017). Characterization of convective plumes associated with oceanic deep convection in the northwestern Mediterranean from high resolution in-situ data collected by gliders. *Journal of Geophysical Research: Oceans*, *122*, 9814–9826. https://doi.org/10.1002/2016JC012633

Marshall, J., & Schott, F. (1999). Open-ocean convection: Observations, theory, and models. *Reviews of Geophysics*, *37*(1), 1–64. https://doi.org/10.1029/98RG02739

Mayot, N., D'ortenzio, F., Taillandier, V., Prieur, L., Pasqueron de Fommervault, O., Claustre, H., . . . Conan, P. (2017). Physical and biogeochemical controls of the phytoplankton blooms in north-western Mediterranean Sea: A multiplatform approach over a complete annual cycle (2012–2013 Dewex experiment). *Journal of Geophysical Research: Oceans*, *122*, 9999–10,019. https://doi.org/10.1002/2016JC012052

McWilliams, J. C. (1985). Submesoscale, coherent vortices in the ocean. *Reviews of Geophysics*, *23*(2), 165–182. https://doi.org/10.1029/RG023i002p00165

MEDOC-Group, T. (1970). Observation of formation of deep water in the Mediterranean Sea, 1969. *Nature*, *225*, 1037–1040. https://doi.org/10.1038/2271037a0

Mortier, L. (2012). *DOWEX2012 cruise, RV Téthys II* (technical report). https://doi.org/10.17600/12450170

Mortier, L., & Taillandier, V. (2013). *DOWEX2013 cruise, RV Téthys II* (technical report). https://doi.org/10.17600/13450150

Pasqueron de Fommervault, O., D'Ortenzio, F., Mangin, A., Serra, R., Migon, C., Claustre, H., . . . Obolensky, G. (2015). Seasonal variability of nutrient concentrations in the Mediterranean sea: Contribution of bio-Argo floats. *Journal of Geophysical Research: Oceans*, *120*, 8528–8550. https://doi.org/10.1002/2015JC011103

Pusceddu, A., Mea, M., Gambi, C., Bianchelli, S., Canals, M., Sanchez-Vidal, A., . . . Danovaro, R. (2010). Ecosystems effects of dense water formation on deep Mediterranean Sea ecosystems: An overview. *Advances in Oceanography and Limnology*, *1(1)*, 67–83.

Schott, F., & Leaman, K. D. (1991). Observations with moored Acoustic Doppler current profilers in the convection regime in the Golfe du Lion, *Journal of Physical Oceanography*, *21*, 558–574. https://doi.org/10.1175/1520-0485(1991)021<0558:OWMADC>2.0.CO;2

Schott, F., Visbeck, M., Send, U., Fischer, J., Stramma, L., & Desaubies, Y. (1996). Observations of Deep Convection in the Gulf of Lions, Northern Mediterranean, during the Winter of 1991/92. *Journal of Physical Oceanography*, *26*, 505–524. https://doi.org/10.1175/1520-0485(1996)026<0505:OODCIT>2.0.CO;2

Send, U., & Marshall, J. (1995). Integral effects of deep convection. *Journal of Physical Oceanography*, *25*(5), 855–872. https://doi.org/10.1175/1520-0485(1995)025 <0855:IEODC >2.0.CO;2

Somot, S., Houpert, L., Sevault, F., Testor, P., Bosse, A., Taupier-Letage, I., . . .Hermann, M. (2016). Characterizing, modelling and understanding the climate variability of the deep water formation in the north-western Mediterranean sea. *Climate Dynamics*, 1–32. https://doi.org/10.1007/s00382-016-3295-0

Somot, S., Sevault, F., & Déqué, M. (2006). Transient climate change scenario simulation of the Mediterranean Sea for the twenty-first century using a high-resolution ocean circulation model. *Climate Dynamics*, *27*(7–8), 851–879. https://doi.org/10.1007/s00382-006-0167-z

Stabholz, M. Durrieu de Madron, X., Canals, M., Khripounoff, A., Taupier-Letage, I., Testor, P., . . . Dennielou, B. (2013). Impact of open-ocean convection on particle fluxes and sediment dynamics in the deep margin of the Gulf of Lions. *Biogeosciences*, *10*(2), 1097–1116. https://doi.org/10.5194/bg-10-1097-2013

Tamburini, C., M., Canals, X., Durrieu de Madron, L., Houpert, D., Lefvre, S., Martini, A., . . . Zúñiga, J. (2013). Deep-sea bioluminescence blooms after dense water formation at the ocean surface. *PLoS One*, *8*(7), e67523.

Taupier-Letage, I. (2013). *Temperature, Salinity and Density (CTD) vertical profiles during HyMeX SOP1* (technical report). https://doi.org/10.6096/MISTRALS-HYMEX.CTD_SOP1.20130610

Taupier-Letage, I., & Bachelier, C. (2013). *CTD_SOP2, Provence - Tethys 2* (technical report). https://doi.org/10.6096/MISTRALS-HyMeX.950

Testor, P. (2013). *DEWEX-MERMEX 2013 LEG1 cruise, RV Le Suroît* (technical report). https://doi.org/10.17600/13020010

Testor, P., Coppola, L., & Mortier, L. (2012). *MOOSE-GE 2012 cruise, RV Le Suroît* (technical report). https://doi.org/10.17600/12020030

Testor, P., Coppola, L., & Mortier, L. (2013). *MOOSE-GE 2013 cruise, RV Téthys II* (technical report). https://doi.org/10.17600/13450110

Testor, P., Durrieu de Madron, X., Mortier, L., D'ortenzio, F., Legoff, H., Dausse, D., . . . Houpert, L. (2016). *LION observatory data*, *SEANOE* (technical report). http://doi.org/10.17882/44411

Testor, P., & Gascard, J.-C. (2003). Large-scale spreading of deep waters in the Western Mediterranean Sea by submesoscale coherent eddies. *Journal of Physical Oceanography*, *33*, 75–87. https://doi.org/10.1175/1520-0485(2003)033<0075:LSSODW>2.0.CO;2

Testor, P., & Gascard, J.-C. C. (2006). Post-convection spreading phase in the Northwestern Mediterranean Sea. *Deep Sea Research Part I: Oceanographic Research Papers*, *53*(5), 869–893. https://doi.org/10.1016/j.dsr.2006.02.004

Testor, P., Meyers, G., Pattiaratchi, C., Bachmayer, R., Hayes, D., Pouliquen, S., . . .Owens, B. (2010, September 21–25). Gliders as a component of future observing systems. In J. Hall, D. E. Harrison, & D. Stammer (Eds.), *Proceedings of OceanObs'09: Sustained Ocean Observations and Information for Society ESA Publication* (WPP-306, Vol. 2), Venice, Italy. https://doi.org/10.5270/OceanObs09.cwp.89

Thomas, L. N., Tandon, A., & Mahadevan, A. (2008). Sub-mesoscale processes and dynamics. In M. W. Hecht and H. Hasumi (Eds.), *Ocean modeling in an eddying regime, Geophysical Monograph Series* (Vol. 177, pp. 17–38). Washington, DC: American Geophysical Union. https://doi.org/10.1029/177GM04

Visbeck, M., Marshall, J., & Jones, H. (1996). Dynamics of isolated convective regions in the ocean. *Journal of Physical Oceanography*, *26*, 1721–1734. https://doi.org/10.1175/1520-0485(1996)026<1721:DOICRI>2.0.CO;2

Waldman, R., Hermann, M., Somot, S., Arsouza, T., Benshila, R., Bosse, A., . . . Testor, P. (2017a), Impact of the mesoscale dynamics on ocean deep convection: The 2012–2013 case study in the northwestern Mediterranean sea. *Journal of Geophysical Research: Oceans*, *122*, 8813–8840. https://doi.org/10.1002/2016JC012587

Waldman, R., Somot, S., Hermann, M., Bosse, A., Caniaux, G., Estournel, C., . . . Testor, P. (2017b). Modeling the intense 2012–2013 dense water formation event in the northwestern Mediterranean Sea: Evaluation with an ensemble simulation approach. *Journal of Geophysical Research: Oceans*, *122*, 1297–1324. https://doi.org/10.1002/2016JC012437

Waldman, R., Somot, S., Hermann, M., Testor, P., Estournel, C., Sevault, F., . . . Dausse, D. (2016). Estimating dense water volume and its evolution for the year 2012–2013 in the north-western Mediterranean Sea: An observing system simulation experiment approach. *Journal of Geophysical Research: Oceans*, *121*, 6696–6716. https://doi.org/10.1002/2016JC011694

Xing, X., Claustre, H., Blain, S., D'ortenzio, F., Antoine, D., Ras, J., & Guinet, C. (2012). For in vivo chlorophyll fluorescence acquired by autonomous platforms: A case study with instrumented elephant seals in the Kerguelen region (Southern Ocean). *Limnology and Oceanography*, *10*, 483–495. https://doi.org/10.4319/lom.2012.10.483